

Geochemistry, Geophysics, Geosystems®



RESEARCH ARTICLE

10.1029/2023GC010894

Key Points:

- Mantle rocks at Mid Atlantic Ridge Kane recorded complex melt-rock and fluid-rock interactions during incipient mantle exhumation, prior to serpentinization
- Magma channelizing and melt-rock interactions are responsible for metal enrichment (Fe, Co, Zn) in the surrounding mantle silicates
- Metal leaching during hydrothermal alteration of enriched mantle rocks may account for important metal budget at seafloor massive sulfides

Supporting Information:

Supporting Information may be found in the online version of this article.

Correspondence to:

R. Coltat,
remi.coltat54840@gmail.com





Citation:

Coltat, R., Andreani, M., Patten, C. G., Godard, M., Debret, B., & Escartin, J. (2023). Origin of Fe-Ca-metasomatism in exhumed mantle rocks at the MARK area (23°N, ODP Leg 153) and implications on the formation of ultramafic-hosted seafloor massive sulfide deposits. *Geochemistry, Geophysics, Geosystems*, 24, e2023GC010894. <https://doi.org/10.1029/2023GC010894>

Received 2 FEB 2023
Accepted 7 AUG 2023

© 2023 The Authors. *Geochemistry, Geophysics, Geosystems* published by Wiley Periodicals LLC on behalf of American Geophysical Union.
This is an open access article under the terms of the [Creative Commons Attribution-NonCommercial License](https://creativecommons.org/licenses/by-nc/4.0/), which permits use, distribution and reproduction in any medium, provided the original work is properly cited and is not used for commercial purposes.

Origin of Fe-Ca-Metasomatism in Exhumed Mantle Rocks at the MARK Area (23°N, ODP Leg 153) and Implications on the Formation of Ultramafic-Hosted Seafloor Massive Sulfide Deposits

R. Coltat^{1,2} , M. Andreani^{3,4}, C. G. C. Patten⁵, M. Godard⁶ , B. Debret⁷ , and J. Escartin² 

¹Instituto Andaluz de Ciencias de la Tierra, IACT, CSIC-UGR, Armilla, Granada, Spain, ²Laboratoire de Géologie, UMR 8538, Département de Géosciences, Ecole Normale Supérieure de Paris, PSL Research University, Paris, France, ³Laboratoire de Géologie de Lyon, UMR 5672, ENS, Université Lyon 1, Lyon, France, ⁴Institut Universitaire de France, Paris, France, ⁵Institute of Mineralogy and Petrography, University of Innsbruck, Innsbruck, Austria, ⁶Géosciences Montpellier, CNRS, Université de Montpellier, Montpellier, France, ⁷Institut de physique du globe de Paris, CNRS, UMR 7154, Paris, France

Abstract At Mid-Ocean Ridges, hot, reduced, acidic, and metal-rich fluids are responsible for the formation of ultramafic-hosted seafloor massive sulfide deposits (UM-SMSs), where mantle exhumation efficiently operates. As UM-SMSs display great structural, mineralogical, and geochemical variabilities from site to site, a simple genetic model cannot be applied. Notably, fluid circulation and Fe-Ca metasomatism are reported in ultramafic-hosted hydrothermal deposits exposed in ophiolites, suggesting it might have genetic implications on the formation of mineralized systems. Similar Fe-Ca metasomatism was reported in drilled mantle rocks at the Mid Atlantic Ridge Kane (MARK) area, offering access to the vertical dimension beneath an exhumed oceanic core complex to provide an integrative study of the nature and geometry of deep magmatic and hydrothermal processes. At MARK, mantle rocks underwent complex processes of melt-rock and fluid-rock interactions. Magma channeling and interactions with surrounding rocks enriched mantle silicates in Fe, Co, and Zn. There, subsequent hydrothermal alteration allowed to stabilize Fe-rich silicates. Mineralogy and geochemistry of hydrothermal phases at MARK suggest mineral crystallization under temperatures from ~830° down to 350°C during early mantle exhumation at a depth <6.5 km below seafloor, followed by serpentinization of the massif during progressive mantle denudation. Considering the lithological heterogeneity at (ultra)slow-spreading ridges, metal enrichment in deep mantle rocks during melt-rock interactions may be a widespread process. In ultramafic-dominated environments where extensional tectonics allow fluid flows to these deep zones, fluids may leach and transport metals to the surface, accounting for metal entrapment in UM-SMSs.

Plain Language Summary Mantle exhumation along detachment faults is a common tectonic process that efficiently operates at (ultra)slow spreading ridges where the supply of magma is locally insufficient to fully accommodate the lithospheric divergence. This leads to the exposure at seafloor of important volume of deep-seated magmatic and mantle rocks. Detachment faults also represent formidable permeable pathways for fluids, enhancing seawater circulation at depth and fluid-rock interactions with the exhuming rocks. This notably modifies the rheological, thermal, and chemical properties of the oceanic lithosphere and results in a diversity of types of hydrothermal alteration in rocks. At depth, the fluid gets heated (>350°C), decreasing its density and allowing its rise to the seafloor where the mixing with ambient, cold seawater may produce metal-rich sulfide mineralizations. The genetic links between deep-seated hydrothermal alterations and the final venting of the hydrothermal fluid at the seafloor are cryptic because of the difficulty to access these environments.

1. Introduction

Mid-oceanic ridges are associated with hydrothermal fluid circulations in oceanic rocks (i.e., fluid-rock interactions) leading to intense chemical and thermal exchanges between the oceanic lithosphere and the oceans (Alt, 1995). According to the heterogenic nature of the oceanic lithosphere, these result in a diversity of altered rocks and hydrothermal fluids venting at the seafloor (e.g., Kelley et al., 2001; Schwarzenbach & Steele-MacInnis, 2020). High Temperature (HT, >350°C) fluid-rock interactions may produce metal-rich, reduced and acidic fluids

that cause metal precipitation in seafloor massive sulfide deposits (SMS) when mixing with ambient seawater (Alt, 1995; Hannington et al., 2005; Patten et al., 2015; Schwarzenbach & Steele-MacInnis, 2020). SMS form an important diversity of deposits depending on tectonic environments in which they form and the nature of their host rocks (Barrie & Hannington, 1999). Among them, ultramafic-hosted SMS (UM-SMS) have been widely reported in the Atlantic Ocean (Beltenev et al., 2007; Cherkashev et al., 2013; Cherkashov et al., 2008, 2010; Escartin et al., 2017; Fouquet et al., 1998; Krasnov et al., 1995; Melchert et al., 2008) the Indian Ocean (Ding et al., 2020; Kim et al., 2020; Tao et al., 2014; Y. Wang et al., 2014), and the Arctic Mid-Ocean Ridges (Pedersen et al., 2010; Sahlström et al., 2022).

In the last decades, UM-SMS have been studied through direct observations (Cherkashov et al., 2008; Escartin et al., 2017; Fouquet et al., 2008; Ondréas et al., 2012), geophysical methods (Canales et al., 2017; Escartin et al., 2017; McCaig et al., 2007; Ondréas et al., 2012; Petersen et al., 2009; Sztikar et al., 2014), and mineralogical (Hannington et al., 1995; Marques et al., 2006) and geochemical (e.g., Andreani et al., 2014; Charlou et al., 2002; Debret et al., 2018; Marques et al., 2007; Rouxel et al., 2004a, 2004b) approaches. Integration of these results inspired genetic models for the formation of UM-SMSs. In many cases, they suggest a location probably controlled by large off-set faulting (e.g., detachment) that may also control magma emplacement at depth (Fouquet et al., 2010; McCaig et al., 2007; Petersen et al., 2009; Zhao et al., 2012). Some of these models hypothesize that the detachment fault may act as a preferential pathway for hydrothermal fluids allowing both downward and upwards circulation (e.g., McCaig et al., 2007). However, recent seismic data suggests instead that fluids can also circulate within the footwall independently from the detachment fault zone itself. This is the case for the Rainbow hydrothermal field, possibly underlain by magma chambers at depth (Andreani et al., 2014; Canales et al., 2017), the 13°N area, where the Semenov vent field is emplaced on the exposed, inactive detachment (Escartin et al., 2017; Macleod et al., 2009; Mallows & Searle, 2012) or the 14°45'N area, where the formation of the Logatchev hydrothermal field is possibly related to secondary faults (Grevemeyer et al., 2013). More generally, descending fluids are heated at depth thanks to the cooling of magmatic intrusions. There, intense fluid-rock interactions produce acidic, reduced, hot, and metal-rich hydrothermal fluids (e.g., Douville et al., 2002) that flow to the surface and mix with seawater, destabilizing metal complexes to form SMS (e.g., Reed & Palandri, 2006). In ultramafic rocks, this forms typical Cu-Co-Zn(-Au-Ag) mineralizations with variable metal endowment from site to site, that overall contrast with the common Fe ± Cu-Zn mineralizations reported in mafic-hosted deposits (Fouquet et al., 2010). Geochemical signatures of UM-SMSs have been ascribed to the contribution of both mafic and ultramafic reservoirs (e.g., Marques et al., 2006), a scenario locally supported by base metal isotope compositions of mineralization (Debret et al., 2018). Depth constraints of the fluid paths and fluid-rock interactions are scarce and are clearly necessary to better understand and constrain the processes determining the hydrothermal variability observed at UM-SMSs.

The lithological composition and tectonic evolution of the oceanic lithosphere seem to exert a strong control on the nature of the UM-SMSs, according to the important diversity observed in oceanic settings (see Fouquet et al. (2010) for a review) and their fossil record in ophiolites (Melekestseva et al., 2013; Peltonen et al., 2008; see Patten et al., 2022 for a review). Compared to UM-SMSs, ophiolites allow observations to reconstruct the 3D extent and geometries of mineralized systems at depth. Such an approach has been applied in the Alps (Carbonin et al., 2015; Coltat et al., 2019, 2021; Toffolo et al., 2017), and in the Paleoproterozoic Outokumpu thrust belt (Peltonen et al., 2008), documenting the presence of ultramafic-hosted mineralizations that resemble UM-SMSs, except they are closely associated with (Fe-)Ca silicates (e.g., tremolite, diopside, hydro-andradite and ilvaite). Based on mineralogical and geochemical signatures, the Alpine mineralized systems were interpreted as a deep-seated portion of UM-SMS deposits (Coltat et al., 2019; Toffolo et al., 2017). Those examples show that Fe-Ca metasomatism might represent an important deep-seated hydrothermal process related to the formation of UM-SMS, which is virtually invisible in spreading centers due to restricted access to the seafloor but that could be addressed using drill cores at exhumed mantle domes.

Here, we focus on the Mid-Atlantic Ridge Kane (MARK, 23°N) area, an oceanic core complex (Dick et al., 2008) drilled during ODP Leg 153 (Cannat et al., 1995). While UM-SMSs were not reported, Fe-Ca metasomatism and mineralogical assemblages (e.g., ilvaite, hydro-andradite and diopside) were described in recovered mantle rocks (Holes 920B and 920D; Gaggero et al., 1997). Fe-Ca metasomatism occurs either along peridotite-magmatic dykelets contacts or in replacement of the former pyroxenite veins, and is associated with little mineralization (magnetite, pyrite, pyrrhotite, and chalcopyrite; Gaggero et al., 1997). Petrographic and structural features at MARK thus show strong analogies with fossil Alpine systems, suggesting somewhat similar hydrothermal

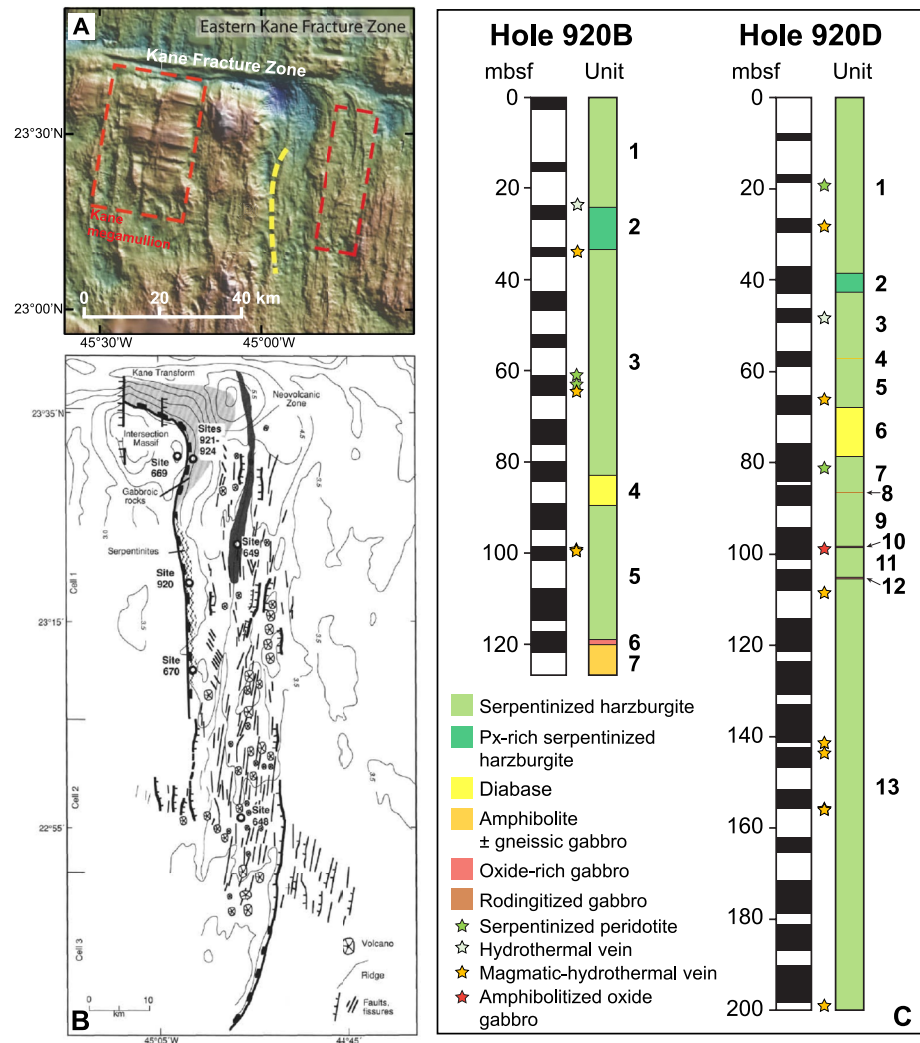


Figure 1. (a) Shaded relief bathymetric map of the Mid-Atlantic Ridge Kane area (after Dick et al. (2010)). The thick yellow dashed line represents the central magnetic anomaly for the Kane megamullion boxed in red on the left side of the map. The two red boxes represent crust from the same age. (b) Zoom on the area where ODP sites are shown as open circles. Shaded areas represent exposed gabbroic rocks, zig-zag line represents the area of serpentinite outcrops, identified from submersible studies and dredging. (c) Lithological logs of the Holes 920B and 920D (after Cannat et al. (1995)). The sample location is displayed.

processes and geological history, even if the latter are more mineralized (Coltat et al., 2019; Toffolo et al., 2017). Hence, the MARK area represents an undisturbed and in situ oceanic system without metamorphism related to late orogenic overprint from Alpine systems. It also offers access to the vertical dimension in mantle rocks, that recorded magmato-hydrothermal processes related to their exhumation from the deep zone to the seafloor at an oceanic core complex, to constrain its potential links with UM-SMS deposition. Using a petrographic and geochemical tracing on mantle and magmatic rocks, we propose to constrain (a) how, when and where Fe-Ca metasomatism occurred during mantle exhumation and (b) what are the chemical mobilities associated with this metasomatism and its implications on the formation of UM-SMS. Besides the above objectives, this study highlights a poorly constrained, likely overlooked, hydrothermal alteration of mantle rocks that might be widespread at slow and ultraslow spreading ridges where mantle exhumation is enhanced.

1.1. Geological Setting at MARK (23°20'N MAR)

The area south to the Kane fracture zone is referred to as the MARK area, 23°N (Figure 1a). The western wall at MARK forms a dome-like uplift (Cannat et al., 1995) corresponding to an inside corner high located on the

southern side of the Kane Fracture Zone at its intersection with the axial rift valley at 23°30'N (Figure 1a). This massif was interpreted as a detachment-related oceanic core complex referring to as the Kane megamullion (Dick et al., 2008). The conjugate crust (i.e., east of MAR) exhibits a deeper bathymetry (>3,500 m), less steep topography and exposes block-faulted basaltic pillow lavas (Cannat et al., 1995). This defines an asymmetric ridge segment, which is a typical feature encountered along the MAR (Tucholke et al., 1998). The axial valley hosts the median neovolcanic ridge that extends 40 km south to the Kane transform (Figure 1b, Cannat et al., 1995) and where the active Snake Pit hydrothermal field lies. The full spreading at MARK is of about 2.5 cm/yr (Schulz et al., 1988).

During ODP Legs 109 (Detrick et al., 1988) and 153 (Cannat et al., 1995), seven sites (669–670; 920–924) were implanted along the western wall at MARK. They mostly yielded mafic rocks, while mantle rocks were recovered at site 920 (ODP Leg 153, Cannat et al., 1994). Site 920 is the focus of this study and is 40 km south to the Kane transform at a depth of ~3,300 m below sea level at 23°20.32'N (Figure 1, Cannat et al., 1994). Two holes were successfully drilled, 920B and 920D, reaching 126 and 200 m below seafloor, with a cumulative recovery of 38% and 47%, respectively (Figure 1c, Cannat et al., 1994). Serpentinized harzburgites were mainly recovered at these holes with minor dunite layers and gabbro veins (Figure 1c). Despite the pervasive serpentinization of mantle rocks, primary textures are well-preserved.

Although HT venting (>350°C) was not reported so far in this off-axis area, oceanic hydrothermalism related to serpentinization played an important role during detachment faulting and mantle exhumation (Andreani et al., 2007; Dilek et al., 1997). This is supported by serpentine vein orientations sub-parallel to the shallow E-dipping fabric. At least five stages of serpentinization linked to the progressive exhumation of deep lithospheric rocks at hole 920 have been identified (Andreani et al., 2007). Isotopic compositions of the MARK serpentinites suggest serpentinization temperatures from >350–400°C down to 200°C (Agrinier & Cannat, 1997; Alt & Shanks, 2003; Hébert et al., 1990), typical of greenschist metamorphic conditions. However, the presence of talc and cummingtonite in mantle rocks points to a HT hydrothermal event prior to serpentinization (Cannat et al., 1994), suggesting that the thermal regimes during hydrothermalism changed over time. At Holes 920B and 920D, Gaggero et al. (1997) described the unusual Fe–Ca-metasomatism in mantle rocks responsible for the formation of Fe–Ca-rich mineral phases (ilvaite, hydro-garnet, salitic pyroxene, carbonates, chlorite) close to magmatic veins. This metasomatism was locally accompanied with the formation of oxide (magnetite) and sulfides (pyrite, pyrrhotite, and chalcopyrite) suggesting synchronous metal mobilities in hydrothermal fluids. These assemblages are crosscut by late serpentine veins, suggesting that the former formed during early serpentinization (Gaggero et al., 1997). After petrographic analyses, Gaggero et al. (1997) proposed that primary mantle sulfides were leached during intense serpentinization of mantle rocks and remobilized in hydrothermal fluids. Oxidation of mantle sulfides and sulfur leaching during serpentinization at MARK was also suggested after the high sulfur content (143–1,342 ppm) and redox state (S^{6+} after XANES spectroscopy) of serpentine measured in serpentinized peridotites (Debret et al., 2017).

2. Methods and Sampling

2.1. Sampling Strategy

The studied samples correspond to variably serpentinized and altered mantle and magmatic rocks of Holes 920B and 920D (Table 1). As serpentinization has been previously studied in detail (Andreani et al., 2007; Dilek et al., 1997), we focused here on hydrothermal alteration related to greenschist mineral assemblages and Fe–Ca silicates formation (diopside, hydro-andradite, and ilvaite).

We focused on 19 samples corresponding to four types of petrographic facies: serpentinized peridotites, serpentinized peridotites cut by hydrothermally altered magmatic veins and by hydrothermal veins, and one amphibolitized oxide gabbro (Table 1, Figure 2). The distinction between hydrothermally altered magmatic veins and pure hydrothermal veins is primarily based on core descriptions of ODP Leg 153 (Cannat et al., 1995) coupled to our own microscopic observations. This sample set is representative of the hydrothermal variability observed in mantle rocks at MARK and allows to discuss (a) the conditions of HT hydrothermal alteration after magmatism inception during the exhumation of deep lithospheric rocks, (b) the inheritance of the primary magmatic mineral assemblages and their transformation to secondary minerals, and (c) the chemical mobilities involved during HT hydrothermalism and their implications on the formation of mineral deposits.

Table 1

Description of the Different Mantle and Mafic Rocks of Site 920 (ODP Leg 153, Mid Atlantic Ridge Kane Area) Investigated in This Study

Sample	Depth (mbsf)	Type	Host rock mineralogy	Vein mineralogy	Vein volume	Description
<i>Hole 920B</i>						
920B-3R-1, 2-5 ^{a, b}	23.51	Hydrothermal vein		Srp, Cal, Ccp	100	Amorphous aqua-green Srp vein associated with Cal + Ccp
920B-4R-1, 76-77 ^{a, b}	33.95	Magmatic-hydrothermal vein	Srp, Ol, Opx, Mag, Spl	Srp, Amp, Chl, Tlc	30	Serpentinized peridotite cut by 1.5 cm-thick hydrothermally altered pyroxenite vein
920B-7R-1, 21-22 ^a	61.18	Serpentinized harzburgite	Srp, Mag, Opx, Ol, Spl	Srp	N.A.	Spl-bearing serpentinized harzburgite, different generations of Srp veins
920B-7R-2, 67-68 ^a	63.04	Serpentinized harzburgite	Srp, Mag, Opx, Ol, Spl	Srp	N.A.	Spl-bearing serpentinized harzburgite, different generations of Srp veins
920B-7R-3, 82-84 ^a	64.63	Magmatic-hydrothermal vein	Srp, Mag, Opx	Srp, Amp, Chl	30	Serpentinized peridotite cut by 1cm-thick hydrothermally altered pyroxenite vein
920B-11R-1, 100-108 ^b	99.6	Magmatic-hydrothermal vein	Ol, Srp, Opx, Mag, Spl, Ilv	Amp, Cpx, Chl, Srp, Tlc, Ox, Zr	50	Serpentinized peridotite cut by hydrothermally altered pyroxenite vein
920B-11R-1, 110-119 ^b	99.7	Magmatic-hydrothermal vein	Ol, Opx, Srp, Mag, Spl, Ilv	Cpx, Grt, Chl, Srp	20	Serpentinized peridotite cut by 1 cm-thick hydrothermally altered pyroxenite/gabbro vein
<i>Hole 920D</i>						
920D-3R-2, 4-7 ^a	19.06	Serpentinized dunite	Srp, Mag, Ol	Srp	N.A.	Almost fully serpentinized dunite
920D-4R-1, 80-81 ^{a, b}	28.1	Magmatic-hydrothermal vein	Srp, Mag, Ol	Cpx, Srp, Chl, Amp, Cal, Mag	90	Serpentinized peridotite cut by thick hydrothermally altered pyroxenite/gabbro vein in turn cut by a few mm-thick Cpx + Srp + Mag + Cal veins
920D-6R-2, 28-31 ^{a, b}	48.1	Hydrothermal vein	Srp	Cpx, Srp, Grt, Cal, Po	40	Serpentinized peridotite cut by Cpx-Srp-Grt-Cal-Po vein
920D-8R-1, 12-13 ^a	66.02	Magmatic-hydrothermal vein	Srp, Mag, Ol, Opx, Chl	Chl, Cal, Srp, Sulf	10	Serpentinized peridotite cut by 4mm-thick Chl-rich hydrothermally altered magmatic vein cut in turn by 3mm-thick Cal + Sulf vein
920D-10R-3, 0-4 ^{a, b}	80.96	Serpentinized harzburgite	Srp, Mag, Opx, Ol, Chl, Pl	Srp	N.A.	Spl-bearing serpentinized harzburgite refertilized by minor melt impregnations
920D-12R-3, 96-100 ^{a, b}	98.69	Amphibolitized oxide gabbro	Pl, Cpx, Amp, Chl, Fe-Ti oxide, Mag, Sulf		N.A.	Altered oxide gabbro dyke
920D-13R-4, 5-9 ^{a, b}	108.38	Magmatic-hydrothermal vein	Srp, Mag, Ol	Srp, Chl	5	Serpentinized peridotite cut by 3mm-thick Chl + Srp vein
920D-16R-7, 19-22 ^{a, b}	141.17	Magmatic-hydrothermal vein	Srp, Ol, Mag, Opx	Srp, Chl, Amp, Cpx, Tlc	25	Serpentinized peridotite cut by hydrothermally altered anastomosed pyroxenite/gabbro veins
920D-17R-1, 46-48 ^{a, b}	143.46	Magmatic-hydrothermal vein	Srp, Mag, Ol, Opx	Srp, Amp, Chl, Tlc, Ttn	50	Serpentinized peridotite cut by >2 cm-thick hydrothermally altered gabbro vein
920D-18R-3, 29-33 ^{a, b}	155.64	Magmatic-hydrothermal vein	Srp, Mag, Ol, Opx	Amp, Srp, Cpx	35	Serpentinized peridotite cut by 1.5 cm-thick hydrothermally altered pyroxenite vein
920D-18R-3, 48-54 ^{a, b}	155.83	Magmatic-hydrothermal vein	Ol, Opx, Srp, Mag	Cpx, Srp	10	Serpentinized peridotite cut by >8 mm-thick hydrothermally altered pyroxenite vein
920D-22R-5, 132-141 ^b	194.86	Magmatic-hydrothermal vein	Ol, Opx, Srp, Mag, Ilv, Grt, Amp, Chl, Tlc, Sulf	Cpx, Amp, Srp, Tlc, Chl, Ox	50	Serpentinized peridotite cut by >2 cm-thick hydrothermally altered coarse-grained gabbro vein

Note. serp. = serpentinized, Srp = serpentine, Tlc = talc, Chl = chlorite, Amp = amphibole, Cpx = clinopyroxene, Ol = olivine, Opx = orthopyroxene, Ilv = ilvaite, Grt = hydro-garnet, Zr = zircon, Ttn = titanite, Cal = calcite, Mag = magnetite, Sulf = sulfides, Ccp = chalcopyrite, Po = pyrrhotite, and Ox = oxide. N.A. = not applicable. "Vein volume" denotes the volume of magmatic-hydrothermal and/or hydrothermal veins (serpentine veins are not consider) mixed with the host serpentine in the studied samples. ^a and ^b denote whether the samples were analyzed using bulk rock geochemistry or in-situ LA-IPCMS geochemical analyses, respectively.

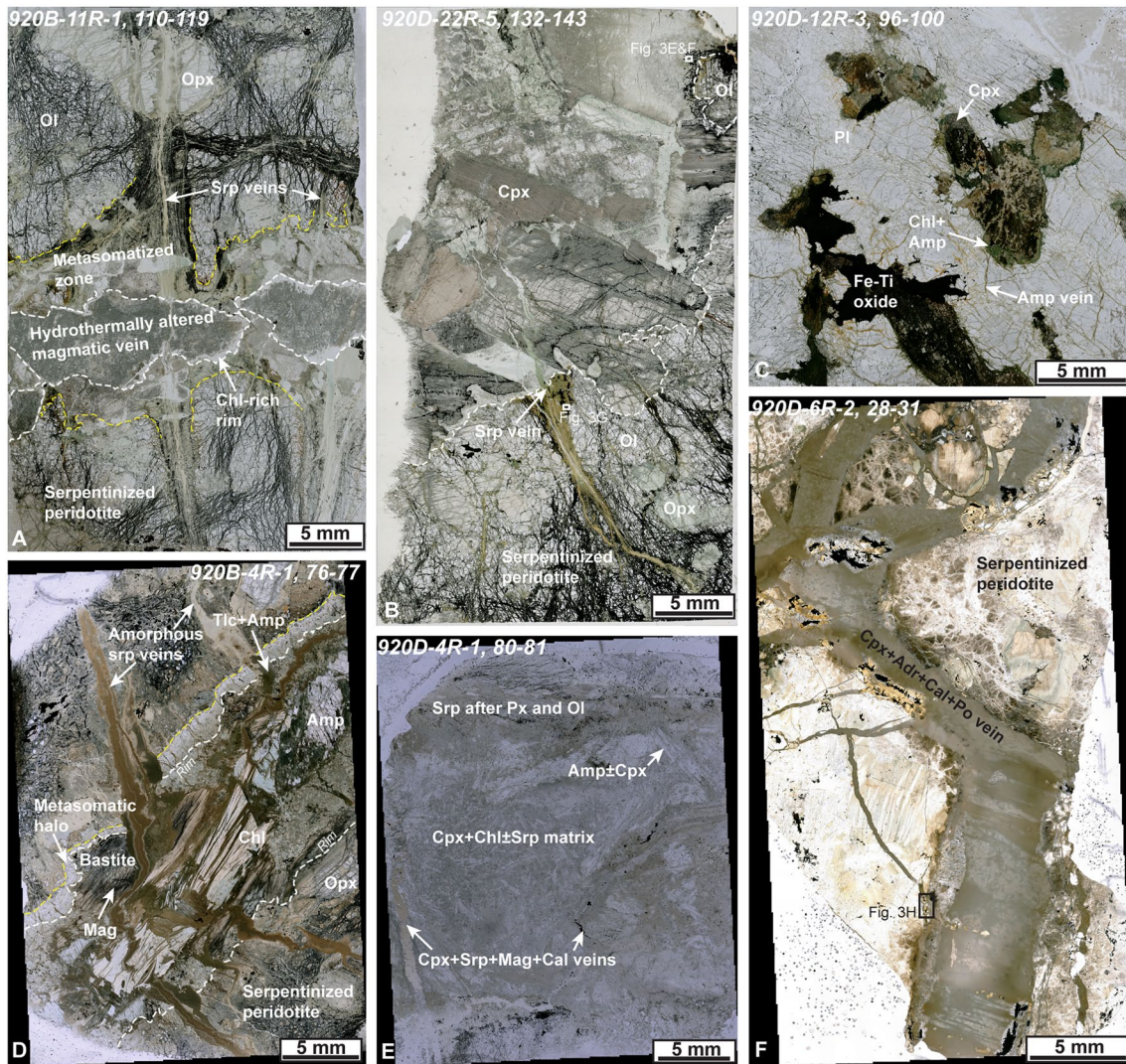


Figure 2. Pictures of mantle and magmatic rocks of the Site 920. (a) Contact between hydrothermally altered magmatic vein and the serpentinized peridotite (sample 920B-11R-1, 110-119). (b) Contact between coarse-grained clinopyroxene-rich magmatic vein and serpentinized peridotite (sample 920D-22R-5, 132-143). (c) Amphibolitized oxide gabbro (sample 920D-12R-3, 96-100). (d) Hydrothermally altered magmatic vein composed of chlorite, amphibole, talc, and serpentine cutting serpentinized peridotite (sample 920B-4R-1, 76-77). (e) Clinopyroxene ± amphibole-rich thick hydrothermally altered magmatic vein cutting serpentinized peridotite. The magmatic vein is crosscut by calcite-diopside-magnetite-serpentine veins (sample 920D-4R-1, 80-81). (f) Hydrothermal vein made of clinopyroxene, hydro-andradite, pyrrhotite, and calcite cutting serpentinized peridotite (sample 920D-6R-2, 28-31). Amp = amphibole, Chl = chlorite, Tlc = talc, Opx = orthopyroxene, Cpx = clinopyroxene, Ol = olivine, Adr = hydro-andradite, Amp = amphibole, Srp = serpentine, Pl = plagioclase, Cal = calcite, Mag = magnetite, and Po = pyrrhotite.

tions (e.g., Rare Earth Element compositions). Nevertheless, we estimated the volume of vein when applicable (Tables 1 and 2). Geochemical compositions of bulk rock and in situ mineral phases are given in Tables 2–5.

2.2. In Situ Mineral (EPMA and LA-ICPMS) Geochemical Analyses

Major and minor element EPMA analyses were performed using a Cameca SX-Five microprobe at the Camparis service (ISTeP, Paris). Spot size of 2 μm , primary beam of 15 kV and 10 nA were set for mineral analyses. The measured elements were Na, Mg, Al, Si, P, K, Ca, Ti, Cr, Mn, Fe, and Ni.

In situ trace element LA-ICP-MS analyses were carried out at the Laboratory of Environment and Raw materials Analysis (LERA), KIT. A Teledyne 193 nm Excimer Laser coupled to an Element XR ThermoFisher ICP-MS was used. Spot size of 35 μm , laser frequency of 10 Hz, fluence of 5 J cm^{-2} and helium and nitrogen flow of 0.3 l min^{-1} and 10 ml min^{-1} , respectively, were set for mineral analysis. Internal standard ^{29}Si from EPMA analyses was used. The following isotopes were measured: ^7Li , ^{29}Si , ^{45}Sc , ^{49}Ti , ^{51}V , ^{53}Cr , ^{55}Mn , ^{57}Fe , ^{59}Co , ^{60}Ni , ^{63}Cu ,

⁶⁶Zn, ⁷⁵As, ⁸⁵Rb, ⁸⁸Sr, ⁸⁹Y, ⁹⁰Zr, ⁹³Nb, ⁹⁵Mo, ¹⁰⁷Ag, ¹¹⁸Sn, ¹²¹Sb, ¹³⁷Ba, ¹³⁹La, ¹⁴⁰Ce, ¹⁴¹Pr, ¹⁴⁶Nd, ¹⁴⁷Sm, ¹⁵¹Eu, ¹⁵⁷Gd, ¹⁵⁹Tb, ¹⁶¹Dy, ¹⁶⁵Ho, ¹⁶⁷Er, ¹⁶⁹Tm, ¹⁷²Yb, ¹⁷⁵Lu, ¹⁷⁸Hf, ¹⁸¹Ta, ²⁰⁵Tl, ²⁰⁸Pb, ²⁰⁹Bi, ²³²Th, ²³⁸U. Calibration and data quality check was done using the USGS standards NIST-612, NIST-614, BHVO-2, BCR-2, and BIR-1. Data reduction was done using Iolite software 3DRS plugin. Accuracy and precision for reference materials (<15% for most elements) as well as limit of detections are detailed in Table S1.

2.3. Bulk Rock Geochemistry

Major element compositions were determined at the SARM-CRPG (Nancy, France; <http://sarm.cnrs.fr>) by Inductively Coupled Plasma Optical Emission Spectroscopy (ICP-OES iCap6500). Trace element concentrations (Li, Sc, Ti, V, Mn, Co, Ni, Cu, Ga, As, Mo, Sn, Sb, Rb, Sr, Y, Zr, Nb, Cs, Ba, Rare Earth Elements (REE), Hf, Ta, Pb, Th, U, W, Tl) were determined at Géosciences Montpellier (AETE-ISO, OSU OREME, University of Montpellier, France) using an Agilent 7700X quadrupole ICP-MS. Unignited powder samples were analyzed after the HF/HClO₄ digestion procedure of Ionov et al. (1992) using the measurement protocol described in Godard et al. (2000). Prior to analysis, solutions were diluted in a 2% HNO₃ solution to a total dilution of 1,000 for unknown samples. An external calibration was used to determine concentrations for most elements. Nb and Ta concentrations were, in contrast, calibrated with internal standards (Zr and Hf concentrations, respectively), a surrogate calibration method adapted from Jochum et al. (1990) to minimize memory effects due to the introduction of concentrated Nb-Ta solutions in the instrument. The Helium cell gas mode of the Agilent 7700X was used to measure Sc, Ti, V, Mn, Co, Ni, Cu, Zn, Ga, As, Sr, Sn, and Sb while removing polyatomic interferences. Each ICP-MS measurement is an average of three runs and its precision is determined by the standard deviation. The uncertainty of analysis was estimated for each sample using an error propagation approach, which considers the precision of the measurements of (a) the instrumental blank, (b) the procedural blanks and (c) the sample analysis. Analyses (a) below the instrument detection limit, (b) for which the contribution of the procedural blank is >70% or (c) having uncertainties >50% were eliminated (noted “not determined”). The external precision and accuracy of analyses was assessed by repeated analyses of certified reference materials: serpentinite UB-N, peridotite JP-1, and basalt BIR-1. The limit of detection of the instrument, the average values of the procedural blanks and rock standards obtained during this study are reported in Table S2.

3. Results

3.1. Petrography of the MARK Serpentinized Peridotites and Oxide Gabbro

Samples investigated in this study mainly correspond to variably serpentinized peridotites (harzburgite and dunite) locally cut by hydrothermally altered magmatic veins (gabbro or pyroxenite) and hydrothermal veins (Figures 2 and 3). A single sample corresponds to an amphibolitized oxide gabbro (Figure 2c). Serpentinized peridotites and magmatic rocks at the MARK area display a great variability of mineralogical assemblages, textural relationships and petrographic habits (e.g., vein infills, coronitic alteration, pervasive replacement). We present here the petrographic features of the host rocks and then the main secondary hydrothermal paragenesis encountered in these rocks.

3.1.1. Serpentinized Peridotites

Serpentinized peridotites display a translucent to greenish aspect with a darker aspect in magnetite-rich areas (Figures 2a and 2b). They display a weakly to moderately foliated porphyroclastic texture, generally carried by magnetite. Most of the time, this fabric is crosscut by different generations of serpentine veins, while some veins may be parallel to it. Olivine is partly to completely replaced by serpentine and magnetite, and appears more preserved at the contact with magmatic veins. Orthopyroxene forms coarse and translucent grains (up to 1.5 cm) that may present a green corona. In the most altered samples, orthopyroxene is entirely replaced by serpentine, chlorite, and possibly clay minerals. Spinel (<1% total rock volume) up to 2 mm was observed either associated with pyroxene or in the serpentine groundmass.

Serpentinization occurs as pseudomorphic textures, forming typical mesh and bastite textures after olivine and orthopyroxene, respectively. Mg-Lizardite is the main serpentine species observed, according to previous petrographic studies (e.g., Andreani et al., 2007; Dilek et al., 1997; Rouméjon & Cannat, 2014). Brucite was not observed but its recognition is difficult due to fine-grained serpentine-brucite intergrowths (Dilek et al., 1997). Magnetite is commonly found in the mesh rims and around spinel, while it is nearly absent in pyroxene. Besides magnetite, tiny (<50 μm) sulfides (<1% of the total rock volume), mainly pentlandite and pyrrhotite (and minor

Table 2

Bulk Rock Chemical Compositions of Serpentinized Peridotites and Mafic Rocks of the Mid Atlantic Ridge Kane Area

Petrographic facies	Serpentinized harzburgite			Serpentinized dunite	Serpentinized peridotites cut by hydrothermal veins			
	920B-7R-1, 21-22	920B-7R-2, 67-68	920D-10R-3, 0-4	920D-3R-2, 4-7	920B-3R-1, 2-5	920D-6R-2, 28-31	920B-4R-1, 76-77	920B-7R-3, 82-84
Vein volume (%)					100	40	30	30
Major element (wt. %)								
SiO ₂	41.34	41.27	38.81	39.02	40.3	44.11	41.96	38.36
Al ₂ O ₃	1.30	0.96	0.98	0.79	1.51	0.74	3.54	1.07
MgO	34.72	35.42	37.29	38.08	36.72	29.97	34.41	38.31
CaO	1.84	2.04	0.18	b.d.1	0.44	7.21	1.99	b.d.1
Fe ₂ O ₃ ^a	7.22	6.46	8.33	7.63	6.04	7.01	8.35	8.87
MnO	0.15	0.14	0.13	0.085	0.15	0.13	0.13	0.11
TiO ₂	b.d.1	b.d.1	0.02	b.d.1	b.d.1	b.d.1	0.028	b.d.1
Na ₂ O	0.09	0.17	0.04	0.08	0.18	0.14	0.14	0.03
K ₂ O	0.03	b.d.1	b.d.1	b.d.1	0.03	b.d.1	0.04	b.d.1
P ₂ O ₅	b.d.1	b.d.1	b.d.1	b.d.1	b.d.1	b.d.1	b.d.1	b.d.1
LOI	12.06	12.8	13.45	13.67	13.98	10.36	8.11	13.09
Total	98.75	99.26	99.23	99.36	99.34	99.67	98.7	99.84
Al ₂ O ₃ /SiO ₂	0.03	0.02	0.03	0.02	0.04	0.02	0.08	0.03
Mg#	0.90	0.92	0.90	0.91	0.92	0.89	0.89	0.90
Trace element (ppm)								
Li	2.04	3.04	1.39	1.89	11.14	30.88	3.53	0.59
Sc	10.3	9.8	7.2	8.2	6.1	68.1	17.1	8.0
V	53	42	33	35	34	305	89	38
Co	90	99	95	117	90	677	116	103
Ni	1788	1629	1897	2427	1175	13,382	2218	2078
Cu	42.4	117.9	4.0	41.1	119.6	247.5	17.5	1.0
Zn	88	53	58	37	126	317	60	46
As	b.d.1	0.07	b.d.1	0.56	0.07	4.24	0.19	b.d.1
Rb	0.399	0.189	0.069	0.220	0.487	0.225	0.372	0.046
Sr	2.4	2.9	1.7	1.8	3.9	6.0	3.1	0.7
Y	0.485	0.438	2.047	0.640	0.096	0.295	15.673	0.407
Zr	0.105	0.305	1.224	0.117	0.052	0.069	15.399	1.338
Nb	0.009	0.009	0.038	0.039	0.009	0.004	0.650	0.027
Cs	0.026	0.012	0.003	0.010	0.039	0.011	0.028	0.001
Ba	0.620	0.207	0.129	0.262	1.152	0.540	0.496	0.158
Hf	0.0062	0.0109	0.0398	0.0049	0.0030	0.0035	0.7721	0.0384
Ta	0.0005	0.0004	0.0023	0.0016	0.0003	0.0002	0.0429	0.0006
Pb	7.713	11.089	2.801	0.520	0.222	6.415	1.943	13.937
Th	0.0009	0.0007	0.0017	0.0019	0.0004	0.0003	0.1793	0.0037
U	0.002	0.006	0.002	1.346	0.009	0.146	0.013	0.005
Mo	0.050	0.064	0.037	1.148	0.026	0.217	0.252	0.037
Sn	0.407	0.057	0.101	0.130	0.073	0.109	0.303	0.126
Sb	0.053	0.035	0.006	0.125	0.043	0.073	0.015	0.010
REE (ppm)								
La	0.0167	0.0288	0.1648	0.0837	0.0315	0.0110	0.8793	0.1149
Ce	0.0335	0.0470	0.5344	0.2171	0.0480	0.0127	4.7620	0.3662
Pr	0.0046	0.0060	0.1003	0.0358	0.0056	0.0024	1.0130	0.0558
Nd	0.0206	0.0283	0.5710	0.1860	0.0139	0.0075	5.8121	0.2459
Sm	0.0086	0.0101	0.1952	0.0591	0.0028	0.0053	1.9616	0.0408
Eu	0.3228	0.0259	0.2487	0.0979	0.0318	0.2027	0.1750	0.0987
Gd	0.0267	0.0234	0.2696	0.0627	0.0045	0.0154	2.3565	0.0464
Tb	0.0071	0.0062	0.0477	0.0126	0.0013	0.0045	0.4266	0.0075
Dy	0.0711	0.0570	0.3437	0.0953	0.0104	0.0434	2.8506	0.0629
Ho	0.0191	0.0161	0.0768	0.0226	0.0034	0.0110	0.6155	0.0147
Er	0.0726	0.0607	0.2376	0.0738	0.0157	0.0387	1.8854	0.0468
Tm	0.0124	0.0106	0.0371	0.0135	0.0029	0.0069	0.2883	0.0079
Yb	0.0943	0.0852	0.2604	0.0998	0.0272	0.0527	1.9406	0.0582
Lu	0.0170	0.0150	0.0443	0.0165	0.0062	0.0088	0.2949	0.0105

Note. "Vein volume" denotes the volume of hydrothermal and/or hydrothermally overprinted magmatic veins (serpentine veins are not considered) mixed with the host serpentinite in the studied samples. Not applicable for serpentinized peridotites and amphibolitized gabbro.

^aTotal Fe as Fe₂O₃, b.d.1 = below detection limits.

Serpentinized peridotites cut by hydrothermally altered magmatic veins							Amphibolitized gabbro
920D-4R-1, 80-81	920D-8R-1, 12-13	920D-13R-4, 5-9	920D-16R-7, 19-22	920D-17R-1, 46-48	920D-18R-3, 29-33	920D-18R-3, 48-54	920D-12R-3, 96-100
90	10	5	25	50	35	10	
44.94	38.84	39.09	38.8	44.67	41.36	38.61	48.09
2.52	1.84	1.09	0.84	9.12	1.18	1.24	15.75
26.24	35.07	37.15	36.48	20.93	33.75	36.55	6.31
10.36	2.61	0.21	0.14	8.04	3.17	0.84	12.64
8.21	8.08	8.79	11.24	10	10.15	10.85	9.73
0.19	0.17	0.13	0.21	0.14	0.18	0.13	0.2
0.024	0.066	b.d.1	b.d.1	0.2	0.038	0.049	0.29
0.2	0.07	0.05	0.04	0.91	0.13	0.03	2.92
b.d.1	b.d.1	b.d.1	b.d.1	0.04	b.d.1	b.d.1	0.08
b.d.1	b.d.1	b.d.1	b.d.1	b.d.1	b.d.1	b.d.1	b.d.1
7.03	13.65	12.71	12.07	5.55	9.88	10.9	3.58
99.71	100.4	99.21	99.81	99.6	99.84	99.21	99.57
0.06	0.05	0.03	0.02	0.20	0.03	0.03	0.33
0.86	0.90	0.89	0.87	0.81	0.87	0.87	0.56
4.34	2.92	15.92	1.89	5.67	1.90	0.98	4.49
9.2	10.1	9.1	8.8	6.5	7.2	12.0	36.9
99	55	50	35	124	48	60	110
92	88	103	95	60	87	104	30
2071	1711	2039	1691	1569	1446	1801	96
18.8	23.9	5.6	1.9	0.5	3.5	23.9	19.6
41	59	44	39	41	36	50	102
0.47	b.d.1	b.d.1	b.d.1	0.12	b.d.1	b.d.1	0.22
0.170	0.175	0.093	0.059	0.112	0.109	0.033	0.217
3.2	13.5	1.5	1.0	6.1	1.9	1.3	198.9
39.068	1.682	2.193	2.494	16.100	5.821	1.799	36.883
7.718	3.409	0.427	1.442	30.972	2.417	2.786	17.969
1.113	0.230	0.079	0.219	2.195	0.305	0.055	0.165
0.012	0.011	0.004	0.002	0.003	0.005	0.001	0.007
1.133	0.829	0.134	0.410	0.286	0.290	1.383	7.037
0.2260	0.0994	0.0266	0.0569	1.5075	0.0804	0.0861	0.7839
0.0986	0.0133	0.0049	0.0128	0.2248	0.0091	0.0044	0.0156
2.235	7.761	0.493	7.286	0.457	0.055	2.498	1.844
0.1862	0.0172	0.0171	0.0602	0.0375	0.0561	0.0028	0.0216
0.019	0.006	0.005	0.009	b.d.1	0.006	0.002	0.058
0.034	0.044	0.031	0.043	0.027	0.054	0.046	0.284
1.281	0.077	0.119	0.072	0.584	0.348	0.043	0.658
0.009	0.028	0.009	0.011	0.030	0.003	0.007	0.006
2.8389	0.1238	0.1976	0.2300	0.8406	0.5891	0.0768	2.3802
16.8746	0.4826	0.7914	0.9653	4.0432	2.8740	0.2623	7.7141
3.5865	0.0915	0.1394	0.1758	0.8299	0.5782	0.0495	1.4078
20.0784	0.4971	0.6950	0.8877	4.7642	3.1694	0.2869	8.1784
6.1593	0.1670	0.2042	0.2682	1.7194	0.9717	0.1197	3.1246
1.1721	0.1049	0.0479	0.1008	0.7427	0.3414	0.0490	2.3816
6.6799	0.2224	0.2524	0.3187	2.2212	1.0970	0.1978	4.5553
1.1522	0.0424	0.0503	0.0607	0.4192	0.1846	0.0392	0.8513
7.5794	0.3015	0.3725	0.4341	2.8931	1.2098	0.3001	6.0662
1.5965	0.0674	0.0879	0.0983	0.6259	0.2524	0.0722	1.3450
4.7848	0.2100	0.2956	0.3237	1.8982	0.7577	0.2337	4.0745
0.7378	0.0343	0.0501	0.0540	0.2801	0.1138	0.0378	0.6278
4.8737	0.2294	0.3724	0.3832	1.7970	0.7790	0.2703	4.2684
0.7184	0.0381	0.0608	0.0622	0.2718	0.1217	0.0447	0.6647

3.1.3. Hydrothermally Altered Magmatic Veins and Contact With Serpentinized Peridotite

Twelve samples correspond to serpentinized peridotites cut by different types of millimeter to >centimeter thick magmatic veins that display partial to complete alteration to secondary hydrothermal minerals (Table 1, Figures 2a, 2b, 2d, and 2e). Hydrothermally altered magmatic veins form white, gray, and green veins that in some instances are cut by serpentine veins (Figures 2a, 2b, and 2d). This suggests that serpentinization lasted after magmatic veining and hydrothermal alteration of igneous minerals. A white to greenish millimetric halo may develop at the contact with the host serpentinized peridotite (Figures 2a and 2d).

In partly altered veins, the igneous mineralogy mainly consists of clinopyroxene that form sub-millimetric to centimetric translucent grains (Figure 2b), while primary plagioclase was never observed. Zircon was observed in one vein (920B-11R-1, 100-108; Table 1). Secondary hydrothermal mineral assemblages are complex and their mode and proportions vary from vein to vein. Notably, one magmatic vein (920B-11R-1, 110-119) shows complete replacement of igneous minerals to secondary clinopyroxene (diopside composition, Figures S1b–S1d in Supporting Information S1), hydro-grossular, chlorite, and minor serpentine (Table 1, Figures 2a and 3b). Chlorite becomes more abundant and Fe-rich toward the rims (Figure 3b). Other magmatic veins are commonly composed of clinopyroxene-amphibole-chlorite-serpentine-talc-(titanite) assemblages in variable proportions (Table 1, Figures 2b, 2d, 2e, 3c, and 3d). Titanite was only observed in one vein associated with chlorite (920D-17R-1, 46-48; Table 1). Clinopyroxene is either partially altered to serpentine and magnetite along the cleavage planes (Figure 2b) or replaced by amphibole (Figure 3c). Amphibole and phyllosilicates may form a groundmass of tiny imbricated crystals (interstratified?), although coarser amphibole and chlorite grains (up to 1 cm) were also observed (Figures 2d and 3c). There, it is common to observe chemical zonation; chlorite shows variable FeO and MgO contents and amphibole shows variable Al_2O_3 and Na_2O contents.

At the contact between the former magmatic veins and the serpentinized peridotite, mantle silicates are preserved from extensive serpentinization. In some instances, a metasomatic halo made of talc, chlorite, amphibole, clinopyroxene, serpentine, and minor ilvaite and hydro-andradite is present (Figures 3e–3g). Ilvaite and hydro-garnet show textural equilibrium with amphibole (and possibly clinopyroxene), forming local fiber-like textures of hydro-garnet and amphibole enclosed in a talc-chlorite groundmass (Figure 3e). Ilvaite was observed in three samples (920B-11R-1, 100-108; 920B-11R-1, 110-119; 920D-22R-5, 132-143, Table 1) and either occurs around sulfides and oxides (Figure 3f) or replaces Fe-rich olivine along grain boundaries and fractures (ilvaite, Figure 3g). The latter does not show evidence of recrystallization. Ilvaite and hydro-andradite may be associated with deep green Fe-serpentine, differing from common Mg-lizardite observed in serpentinized peridotite away from magmatic veins.

3.1.4. Hydrothermal Veins

Two serpentinized peridotites are cut by hydrothermal veins of variable mineralogy (Figure 2f, Table 1). In one sample (920D-6R-2, 28-31, Table 1), the serpentinized peridotite is cut by large anastomosed veins (up to 1 cm) made of clinopyroxene (diopside in composition, Figure S1d in Supporting Information S1), hydro-andradite, calcite, serpentine, and pyrrhotite (Figures 2f and 3h). The vein presents a turbid groundmass of clinopyroxene grains that surround clasts made of hydro-andradite, serpentine, pyrrhotite, and calcite, suggesting late crystallization of diopside. Serpentine either surrounds or fills fractures cutting through hydro-andradite, supporting it replaces hydro-andradite (Figure 3h).

Somehow similar sub-millimetric to millimetric veins composed of diopside, serpentine, calcite, and magnetite cut through hydrothermally altered magmatic veins (920D-4R-1, 80-81 and 920D-8R-1, 12-13, Table 1).

Another sample (920B-3R-1, 2-5, Table 1) consists of aqua-green amorphous serpentine vein, crosscut by a few calcite veins associated with tiny (<50 μm) chalcopyrite grains. In this sample, relics of primary mantle minerals (e.g., olivine, pyroxene) are absent, suggesting a veining process rather than replacement of the former peridotite. More generally, the presence of sulfides in these veins suggests metal mobilization during veining.

3.2. Bulk Rock Geochemistry of Mantle and Magmatic Rocks

3.2.1. Major Elements and Metal Compositions

The studied samples display chemical compositions that commonly lie between the poles defined by the serpentinized peridotites and mafic rocks at MARK, and overlap the range defined by the MARK pyroxenites (Figure 4).

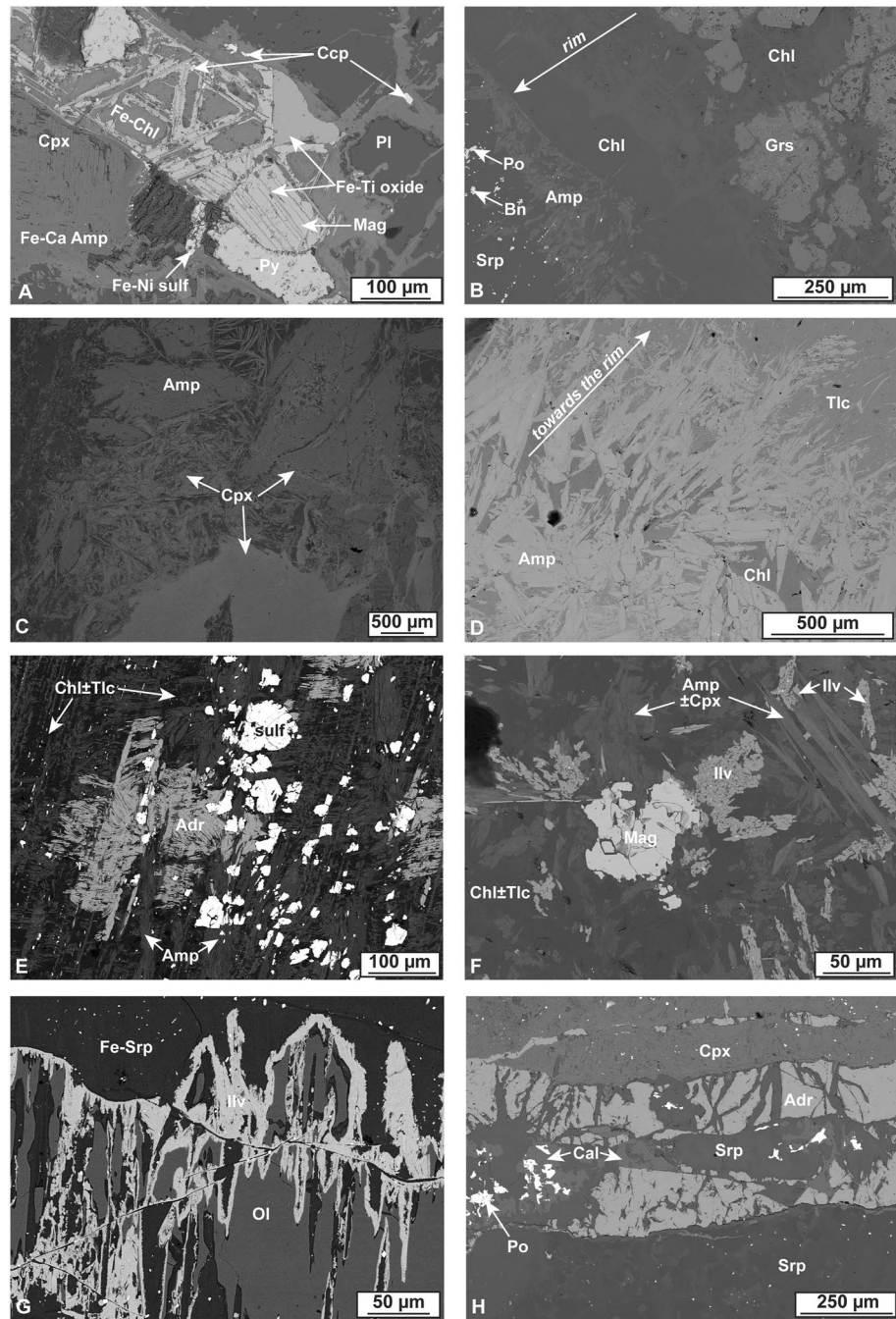


Figure 3. SEM pictures of mantle and magmatic rocks of Site 920. (a) Magmatic vein altered to chlorite and hydro-grossular and showing chlorite enrichment toward the rims (920B-11R-1, 110-119). (b) Amphibolitized oxide gabbro (920D-12R-3, 96-100). Amphibole and Fe-chlorite form at the expense of clinopyroxene and Fe-Ti oxide, respectively. Secondary Cu-rich sulfide forms together with amphibole. (c) Hydrothermally altered magmatic vein composed of clinopyroxene, amphibole, serpentine, and chlorite (920D-18R-3, 29-33). (d) Talc-chlorite-amphibole assemblages in hydrothermally altered magmatic vein (920D-17R-1, 46-49). The proportion of talc increases toward the rim of the vein. (e-g) Contact between hydrothermally altered coarse-grained gabbro vein and the serpentinized peridotite (920D-22R-5, 132-141). (e) Hydro-andradite forming fibrous-like texture around sulfides and is associated with amphibole, chlorite, talc. (f) Ilvaite replacing magnetite and associated with amphibole in a fine-grained matrix of chlorite + talc. (g) Ilvaite replacing olivine and surrounded by a matrix of Fe-serpentine. (h) Hydrothermal vein made of hydro-andradite, clinopyroxene, serpentine, pyrrhotite, and calcite cutting through serpentinized peridotite (920D-6R-2, 28-31). Amp = amphibole, Chl = chlorite, Tlc = talc, Cpx = clinopyroxene, Adr = hydro-andradite, Grs = hydro-grossular, Ol = olivine, Ilv = ilvaite, Srp = serpentine, Pl = plagioclase, Cal = calcite, Po = pyrrhotite, Ccp = chalcopyrite, Py = pyrite, Bn = bornite, Mag = magnetite, and sulf. = sulfides.

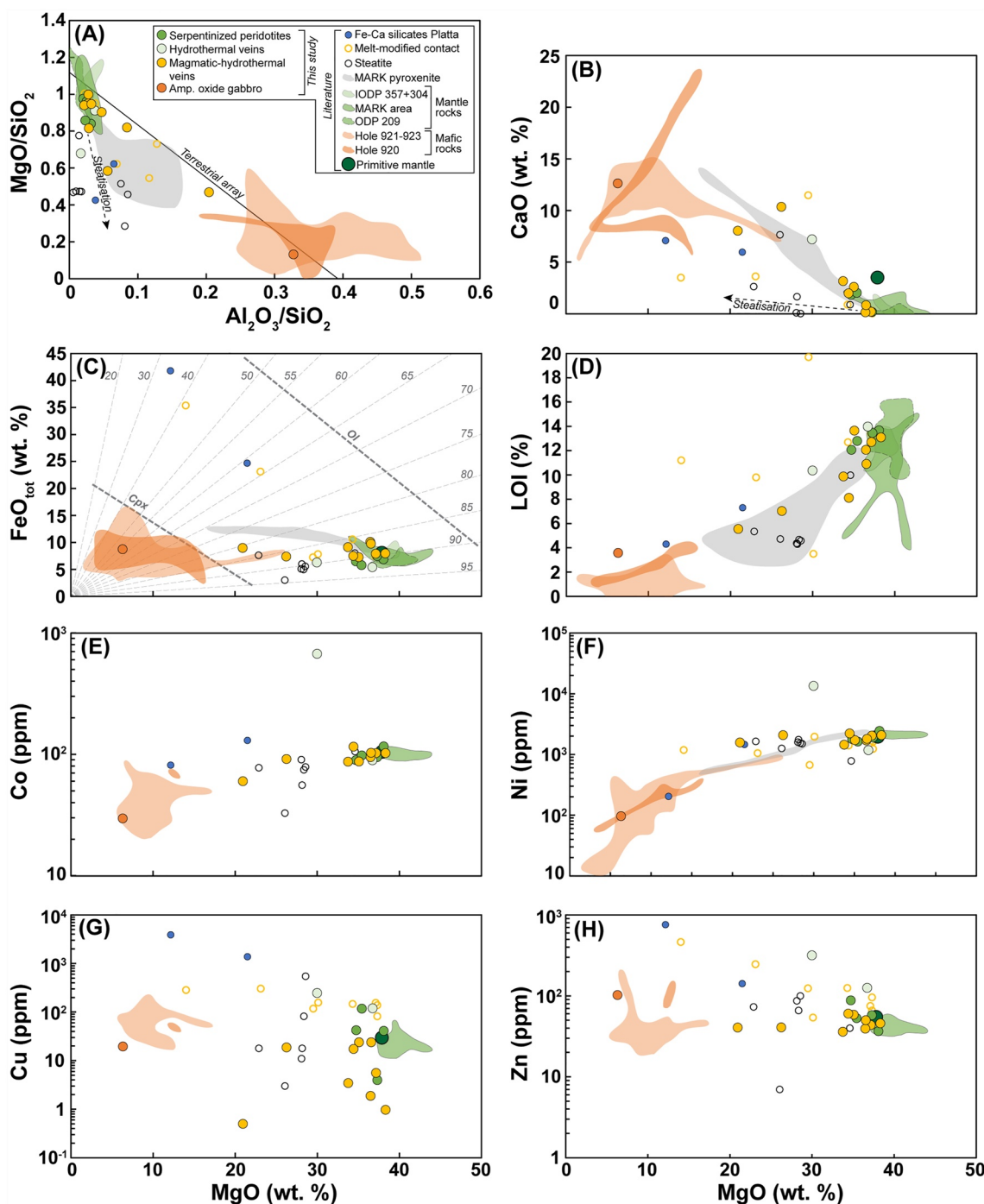


Figure 4. Bulk rock major and trace element chemical compositions of mantle and mafic rocks of Site 920 plotted along with data of Fe-Ca silicates of the Platta nappe (Coltat et al., 2021), melt-modified contacts at the Kane megamullion (Ciazela et al., 2018), abyssal steatite (Delacour et al., 2008; Früh-Green et al., 2018; Paulick et al., 2006), Mid Atlantic Ridge Kane (MARK) pyroxenite and mafic rocks (Casey, 1997), MARK serpentinized peridotites (Burgath et al., 1997; Casey, 1997; Stephens, 1997; Werner & Pilot, 1997), IODP 357 + 304 (Delacour et al., 2008; Früh-Green et al., 2018), ODP Leg 209 (Godard et al., 2008; Paulick et al., 2006). (a) MgO/SiO₂ versus Al₂O₃/SiO₂. (b–d) CaO, FeO, and LOI versus MgO wt.%, respectively. (e–h) Co, Ni, Cu, Zn (ppm) versus MgO wt. %, respectively. The black line in panel (a) represents the bulk silicate earth evolution (after Jagoutz et al. (1979)). The dashed lines in panel (c) represent iso-Mg# lines for Mg# (= 100*molar(Mg/(Fe + Mg))).

Serpentinized peridotites have high MgO/SiO₂ ratio, LOI, MgO and low CaO contents, similar to those of abyssal serpentinized peridotites elsewhere. The MgO/SiO₂ ratio and LOI decrease, and the CaO content increases in other samples compared to serpentinized peridotites. Serpentinized peridotites cut by hydrothermally altered magmatic veins display high FeO content and low Mg# compared to serpentinized peridotites and serpentinized peridotites cut by hydrothermal veins. The amphibolitized oxide gabbro displays geochemical compositions overlapping those of MARK mafic rocks, but has higher LOI according to the formation of secondary hydrous phases (e.g., chlorite).

Serpentinized peridotites cut by hydrothermal veins (920D-6R-2, 28-31 and 920B-3R-1, 2-5) are enriched in Cu and Zn compared to MARK serpentinized peridotites (Figures 4g and 4h). Sample 920D-6R-2, 28-31 is also enriched in Co and Ni (Figures 4e and 4f). This is in good agreement with the presence of sulfides in these samples. Serpentinized peridotites cut by hydrothermally altered magmatic veins show relative Cu depletion and comparable Zn content than MARK serpentinized peridotites (Figures 4g and 4h).

3.2.2. REE and Extended Trace Element Compositions

Chondrite-normalized REE and primitive mantle-normalized extended trace element compositions of mantle rocks and magmatic rocks at MARK are very heterogeneous, spanning up to three orders of magnitude (Figures 5a–5d).

Serpentinized peridotites and serpentinized peridotites cut by hydrothermal veins display REE and trace element compositions comparable to those of MARK serpentinized peridotites (Figures 5a and 5c), with a strong Eu positive anomaly and a local concave-up shape. This U-shaped pattern is especially well expressed for samples having low CI-normalized Gd/Lu ratios ($Gd/Lu_N < 0.22$). They present a U- and Pb-positive anomaly. Serpentinized peridotites present a positive to negative Sr anomaly and high primitive mantle-normalized (Cs/Th)_N ratios (7.8–114), while serpentinized peridotites cut by hydrothermal vein have strong positive Sr anomaly and high (Cs/Th)_N ratios (132–391).

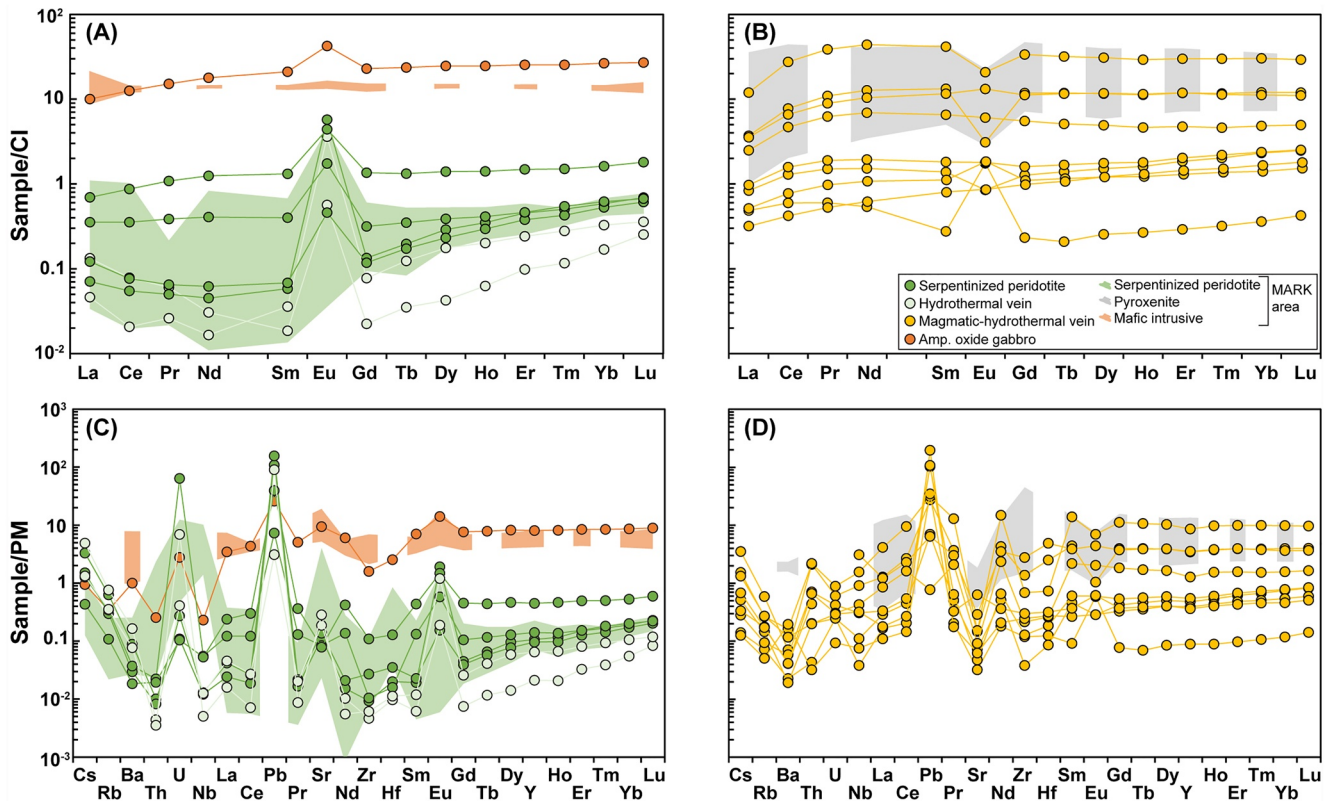


Figure 5. (a, b) CI normalized Rare Earth Elements compositions and (c, d) primitive mantle normalized extended trace element patterns of mantle and magmatic rocks of Site 920 plotted along with data from the literature Burgath et al. (1997) and Casey (1997). Normalizing values are from McDonough and Sun (1995).

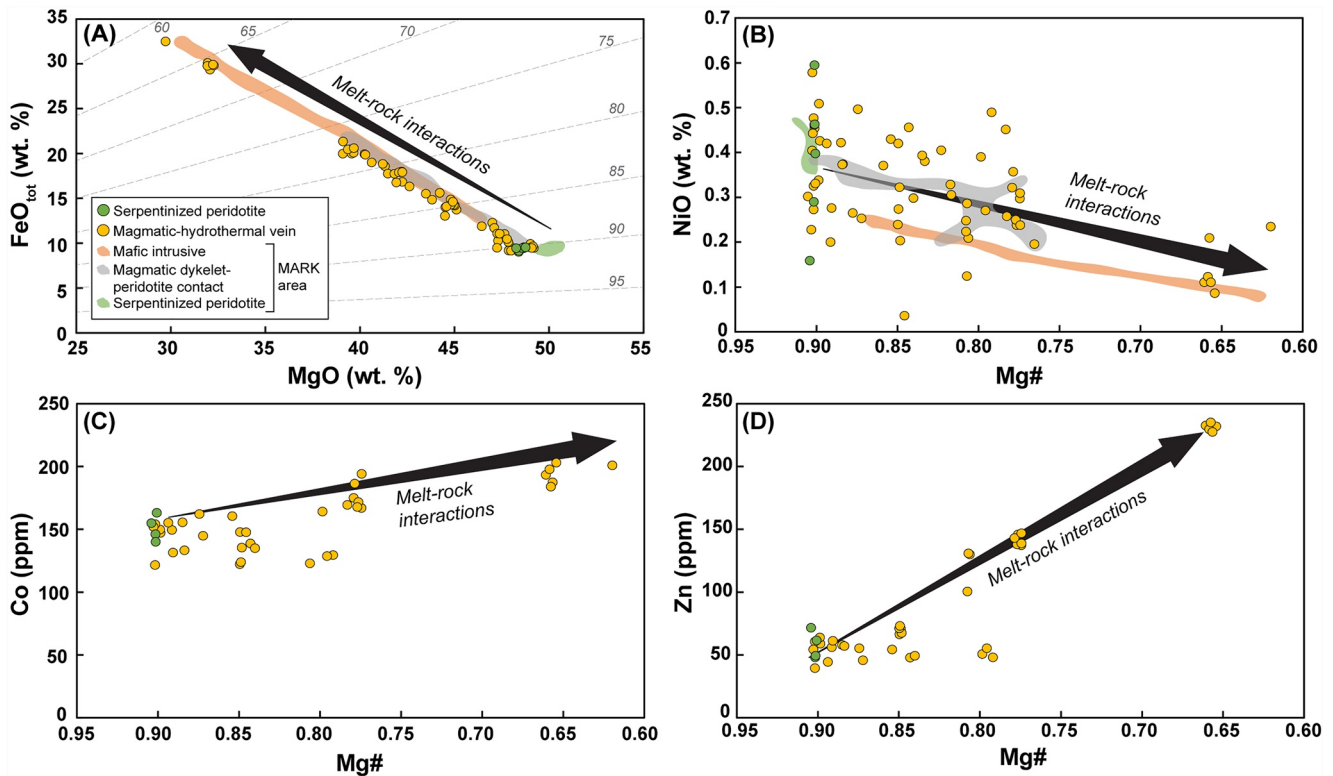


Figure 6. Major and trace element compositions of olivine of Site 920 plotted along with data of the literature Burgath et al. (1997) and Cannat et al. (1997). (a) FeO versus MgO contents in wt. %. They show a negative correlation. The dashed lines represent iso-Mg# lines for Mg#. (b) NiO content in wt. % versus Mg#. (c) Co and (d) Zn content in ppm versus Mg#.

The amphibolitized oxide gabbro shows high REE and trace element compositions with an Eu-positive anomaly, comparable to mafic intrusive rocks recovered at Holes 920B and 920D (Figures 5a and 5c). Notably, it displays low Ba composition, a slight U- and Pb-positive anomaly, and has a low $(\text{Cs}/\text{Th})_N$ ratio (at about 1.3).

Serpentinized peridotites cut by hydrothermally altered magmatic veins display high, even though variable, REE compositions, a positive to negative Eu, U and Pb anomaly, and a generally well-marked Sr-negative anomaly compared to serpentinized peridotites (Figures 5b and 5d). They display a convex up-shaped pattern for LREE and a flat pattern for MREE and HREE (Figure 5b). They have extended trace element patterns that resemble the ones of pyroxenite and/or mafic intrusions at MARK, but they notably present low Ba and Sr compositions (Figure 5d). Compared to serpentinized peridotites, they have low $(\text{Cs}/\text{Th})_N$ ratio (0.14–2.3). A slight positive correlation exists between the vein volume and the La_N composition of these samples (Figure S3 in Supporting Information S1).

3.3. Major, Minor (EPMA), and Trace (LA-ICPMS) Element Mineral Chemistry

3.3.1. Olivine

Olivine displays variable FeO and MgO contents, with higher FeO content (up to 32.5 wt. %) measured in grains at the contact between hydrothermally altered magmatic vein and serpentinized peridotite (920D-22R-5, 132-141; Figure 6a), resulting in a strong decrease of the Mg# (down to 0.62). The latter is accompanied with the decrease of the NiO content (Figure 6b), while the MnO, Y, Co, and Zn contents increase in olivine (Table 3, Figures 6c and 6d) and reach values comparable to those measured in grains of mafic intrusions. There is no evident relationship between the Mg# and the Cu content of olivine (Table 3).

Table 3

Major and Trace Element Compositions of Mantle Olivine at Holes 920B and 920D of the Mid Atlantic Ridge Kane Area

Petrographic facies	Serpentinized harzburgite		Serpentinized peridotites cut by hydrothermally altered magmatic veins															
	920D-10R-3, 0-4 (6)		920B-11R-1, 100-108 (2)		920B-11R-1, 110-119 (7)		920D-4R-1, 80-81 (10)		920D-16R-7, 19-22 (12)		920D-17R-1, 46-48 (6)		920D-18R-3, 29-33 (4)		920D-18R-3, 48-54 (6)		920D-22R-5, 132-141 (14)	
Sample (n)	Mean	2σ	Mean	2σ	Mean	2σ	Mean	2σ	Mean	2σ	Mean	2σ	Mean	2σ	Mean	2σ	Mean	2σ
Major element (wt. %)																		
SiO ₂	41.81	1.00	39.34	0.62	39.54	1.07	40.79	1.12	40.54	2.05	41.67	0.54	41.23	1.09	40.55	0.69	38.51	1.88
Al ₂ O ₃	0.01	0.07	-0.01	0.03	0.01	0.04	-0.01	0.05	-0.01	0.04	0.02	0.03	-0.02	0.03	0.00	0.03	0.00	0.04
MgO	48.53	0.35	40.91	0.83	42.49	1.96	46.13	4.69	45.00	7.02	48.96	0.46	46.63	2.51	44.79	0.41	36.20	8.20
CaO	0.02	0.04	0.02	0.02	0.06	0.05	0.03	0.04	0.02	0.04	0.01	0.04	0.01	0.03	0.03	0.04	0.07	0.05
FeO ^a	9.43	0.30	18.93	0.23	17.20	2.26	12.11	5.96	13.41	9.04	9.51	0.15	12.47	3.35	14.25	0.41	24.51	10.40
NiO	0.39	0.30	0.38	0.31	0.27	0.19	0.35	0.13	0.35	0.21	0.43	0.22	0.35	0.21	0.25	0.26	0.24	0.21
MnO	0.13	0.11	0.27	0.08	0.24	0.08	0.20	0.11	0.21	0.21	0.14	0.12	0.17	0.04	0.19	0.06	0.41	0.44
TiO ₂	0.00	0.03	0.00	0.01	-0.01	0.05	0.01	0.03	0.00	0.04	0.00	0.04	0.00	0.04	0.01	0.03	0.01	0.03
Cr ₂ O ₃	0.00	0.05	-0.02	0.03	-0.01	0.04	0.01	0.05	0.00	0.04	0.00	0.02	0.00	0.07	0.00	0.07	-0.01	0.07
Na ₂ O	0.00	0.03	0.00	0.03	-0.01	0.03	0.00	0.03	0.01	0.03	0.00	0.03	0.01	0.03	0.00	0.03	0.00	0.04
K ₂ O	0.01	0.02	0.00	0.03	0.00	0.01	0.00	0.02	0.00	0.02	0.00	0.01	-0.01	0.00	0.00	0.03	0.00	0.02
P ₂ O ₅	-0.03	0.09	-0.01	0.12	0.00	0.10	0.00	0.07	0.01	0.04	-0.01	0.07	0.00	0.12	0.02	0.12	0.02	0.09
Trace element (ppm)																		
Li	3.93	1.32	6.19	2.67	7.95	2.43	5.23	7.32	2.30	1.20	1.86		2.59	3.31	1.93	0.56	4.11	2.15
Sc	2.41	1.15	1.94	0.84	5.76	0.68	3.43	1.97	3.28	0.44	1.79		5.22	5.85	2.74	0.33	6.79	3.12
Ti	6.30	2.93	9.15	13.9	54.0	29.9	4.29	5.07	5.26	1.95	2.73		24.8	68.5	13.5	7.09	156	226
V	1.32	0.61	1.13	2.20	8.94	1.99	1.43	2.09	1.77	2.46	0.76		5.70	15.75	1.32	0.50	4.61	2.41
Cr	20.8	9.6	12.1	16.1	18.6	2.5	24.6	21.2	32.6	81.8	9.0		102.7	215.5	21.9	10.5	31.1	41.4
Mn	926	84.3	1868	115	1980	70	1400	531	1063	167	815		1595	1251	1227	57	2832	1400
Co	148.8	20.2	185.7	5.0	139.5	28.7	146.6	30.0	152.4	10.7	121.6		146.4	17.1	128.0	10.5	184.3	28.5
Ni	2719	372	2244	33	1470	229	2205	824	2783	156	2241		2429	390	1843	85	1363	684
Cu			0.31	0.57			16.00	18.81	6.13	2.22	0.49		2.11	1.42	0.07	0.03		
Zn	56.4	20.0	51.6	10.4	120.4	34.5	52.8	11.9	58.1	7.3	39.3		50.4	13.0	69.7	5.6	182.4	94.0
As	0.18				0.10		0.22						0.07				0.10	0.00
Rb			0.04		0.16	0.36	0.04	0.04	0.02				0.02	0.02			0.05	0.00
Sr			0.42		1.87	1.97	2.74	0.42	0.43	0.64			1.14	2.78			1.88	0.67
Y	0.04	0.06	0.26	0.57	0.13	0.04	0.09	0.08	0.02	0.02			2.12	5.78	0.02	0.01	0.22	0.30
Zr					0.13	0.04	0.05	0.02					0.21	0.55	0.03	0.01	0.13	0.21
Nb			0.02		0.01		0.10	0.23	0.01	0.01			0.05	0.07	0.00		0.01	0.00
Mo	0.19	0.19	0.77	0.11	0.45	0.13	0.34	0.20	0.44	0.14	0.34		0.70	0.59	0.48	0.08	0.72	0.44
Ag																		
Sn	0.90	0.87	0.31	0.10	0.79	0.11	1.57	1.85	0.28	0.12	0.17		0.35	0.32	0.14	0.03	0.70	0.08
Sb							0.10						0.03					
Ba					0.21	0.34	0.12		0.18				0.09	0.10			0.08	0.13
La			0.02		0.02	0.00	0.01		0.01	0.01			0.07	0.22				
Ce	0.04		0.14				0.11	0.31	0.02	0.02			0.46	1.48	0.00			
Pr			0.03		0.04		0.03	0.04	0.00				0.16	0.42			0.01	
Nd			0.14		0.08		0.05	0.12	0.01				1.59				0.02	
Sm			0.05										0.67					
Eu							0.06						0.15	0.37			0.06	
Gd			0.08										0.30	0.84	0.03			
Tb	0.01		0.01		0.01				0.01	0.01			0.05	0.14			0.01	0.00
Dy	0.07		0.08										0.43	1.14			0.08	0.06
Ho			0.02						0.00				0.07	0.20			0.01	0.01
Er			0.08		0.12	0.02	0.10	0.03	0.01	0.01			0.27	0.67	0.01	0.01	0.12	0.08
Tm			0.01		0.03	0.01	0.03	0.01					0.04	0.08	0.00	0.00	0.03	0.02
Yb	0.03	0.03	0.14		0.22	0.05	0.13	0.15	0.01	0.00			0.27	0.54	0.03	0.03	0.19	0.17
Lu	0.01		0.05		0.06	0.02	0.04	0.04	0.00	0.00	0.00		0.05	0.14	0.01	0.01	0.04	0.04
Hf					0.09												0.04	0.04
Ta							0.00	0.00										
Tl					0.07								0.02					
Pb	0.56	0.54	0.04				0.38	0.44	0.02	0.04	0.09		0.08	0.07	0.03	0.05	0.02	
Bi									0.00	0.00	0.00							
Th			0.03						0.01				0.12	0.31	0.00			
U							0.01	0.02	0.00				0.01	0.01			0.00	

^aTotal Fe as FeO. Blank stand for values below the limits of detection.

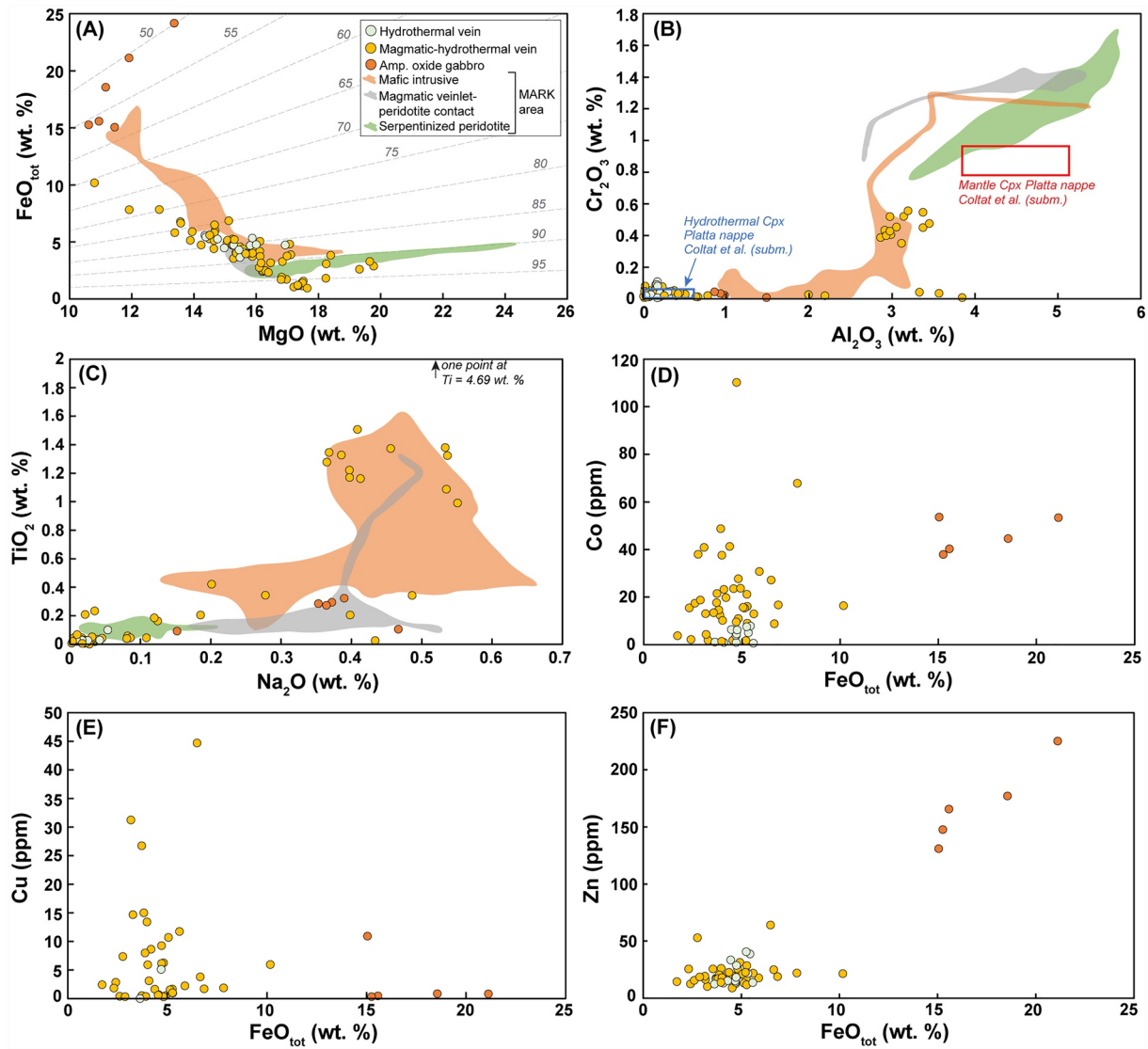


Figure 7. Major and trace element compositions of clinopyroxene of Site 920 plotted along with data of the literature Burgath et al. (1997), Cannat et al. (1997), Stephens (1997), and Werner and Pilot (1997). (a) FeO versus MgO content in wt. %. The dashed lines represent iso-Mg# for Mg#. (b) Cr₂O₃ versus Al₂O₃ contents in wt. %. (c) TiO₂ versus Na₂O contents in wt. %. (d) Co, (e) Cu, and (f) Zn content in ppm versus the FeO content in wt. %.

3.3.2. Clinopyroxene

The FeO and MgO contents of clinopyroxene are scattered (Figure 7a). Regardless of the textural position, most grains have higher FeO content than the serpentinized peridotites at MARK, with the highest values (and lowest Mg#) in clinopyroxene in the amphibolitized oxide gabbro. In hydrothermally altered magmatic veins cutting serpentinized peridotites, FeO and MgO display a negative correlation. There, some grains show high Cr₂O₃, Al₂O₃, TiO₂, and Na₂O contents, overlapping the range defined by mafic intrusions and magmatic veinlet-serpentinized peridotite contacts (Figures 7b and 7c). In veins cutting mantle rocks, the rest of the grains display similar TiO₂ and Na₂O contents and lower Cr₂O₃ and Al₂O₃ contents than those of clinopyroxene in serpentinized peridotites at MARK (Figures 7b and 7c), overlapping the range defined by hydrothermal clinopyroxene of the Platta nappe (Figure 7b). The Co and Zn contents are higher in clinopyroxene in the amphibolitized oxide gabbro than in other samples (Figures 7d and 7f). No direct relationship exists between the FeO and the Cu, Co, and Zn contents in clinopyroxene (Figures 7d and 7f).

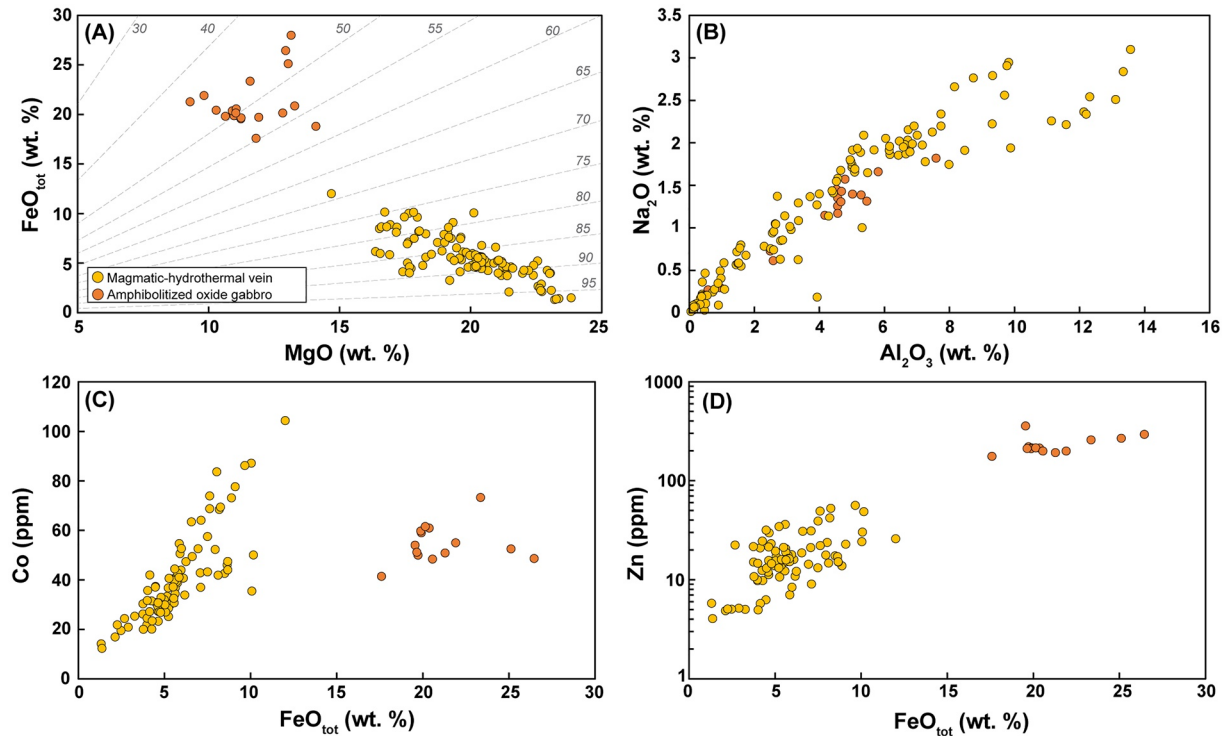


Figure 8. Major and trace element compositions of amphibole of Site 920. (a) FeO versus MgO content in wt. %. The dashed lines represent iso-Mg# for Mg#. (b) Na₂O versus Al₂O₃ contents in wt. %. (c) Co and (d) Zn content in ppm versus the FeO content in wt. %.

3.3.3. Amphibole

In amphibole, FeO and MgO display a negative correlation. Amphibole after clinopyroxene in the amphibolitized oxide gabbro displays higher FeO content compared to other grains (Figure 8a). The Na₂O and Al₂O₃ contents are scattered and positively correlated, with the highest values measured in hydrothermally altered magmatic veins (Figure 8b). Co and Zn display a slight positive correlation with FeO in amphibole in mantle rocks (Figures 8c and 8d). In the amphibolitized oxide gabbro, the Zn content is higher, the Co content is similar, and the Ni content is lower than those of grains in mantle rocks (Figures 8c and 8d, Table 5).

3.3.4. Mineral Pairs

At MARK, fluid-assisted mineralogical transformation includes amphibolitization of clinopyroxene (Figures 9a and 9b), ilvaization of olivine (Figure 9c) and albitization of plagioclase (Figure 9d).

Amphibolitization of clinopyroxene releases Ca in the hydrothermal fluid (Figures 9a and 9b). Regardless the textural position, amphibolitization does not seem to significantly modify the metal budget of the rock as the absolute FeO, Co, Ni, Cu, and Zn contents of amphibole are similar, within the error, to those of clinopyroxene (Tables 4 and 5).

Ilvaization of olivine uptakes Ca and Fe (Figure 9c). Zn seems to be efficiently released in the hydrothermal fluid, while Co and Ni contents are comparable, within the error, between olivine and ilvaite.

Finally, albitization of plagioclase releases Ca in the hydrothermal fluid, while it does not modify its FeO content.

4. Discussion

4.1. A Complex Magmato-Hydrothermal History at the MARK Area

At site 920 at MARK, several lines of evidence plead for complex magmato-hydrothermal processes that produce the different mineral assemblages reported in this study. In the following discussion, we describe these different processes.

Table 4

Major and Trace Element Compositions of Clinopyroxene in Mantle and Magmatic Rocks at Holes 920B and 920D of the Mid Atlantic Ridge Kane Area

Petrographic facies	Serpentinized peridotite cut by hydrothermal vein							
	920D-6R-2, 28-31 (12)		920B-11R-1, 100-108 (9)		920B-11R-1, 110-119 (4)		920D-4R-1, 80-81 (35)	
	Mean	2σ	Mean	2σ	Mean	2σ	Mean	2σ
Major element (wt. %)								
SiO ₂	54.31	0.65	53.15	2.64	53.94	0.63	54.74	1.46
Al ₂ O ₃	0.14	0.16	2.35	2.45	0.58	0.44	0.17	0.40
MgO	15.40	1.46	14.54	3.60	14.59	2.46	16.03	2.94
CaO	24.61	2.06	23.56	1.93	25.27	0.69	25.12	1.60
FeO ^a	4.75	1.17	5.40	2.68	5.65	3.23	3.30	3.96
MnO	0.23	0.28	0.17	0.18	0.34	0.32	0.31	0.52
TiO ₂	0.03	0.05	0.22	0.27	0.03	0.06	0.03	0.04
Cr ₂ O ₃	0.05	0.07	0.02	0.03	0.02	0.01	0.04	0.04
Na ₂ O	0.02	0.03	0.25	0.31	0.02	0.02	0.03	0.06
K ₂ O	0.01	0.02	0.00	0.03	0.01	0.02	0.00	0.02
P ₂ O ₅	0.28	0.11	0.29	0.10	0.30	0.07	0.31	0.09
Trace element (ppm)								
Li	1.20	2.51	2.03	1.76	0.50	0.44	0.62	0.81
Sc	7.63	24.99	14.04	35.47	0.10		3.77	7.92
Ti	74.4	217.4	2196.5	4378.5	146.5	227.1	125.7	266.5
V	22.32	41.15	117.44	162.95	9.48	8.28	81.26	141.96
Cr	156.0	280.7	205.2	480.8	1.4		294.7	742.7
Mn	1943	1499	1120	1110	2448	1647	1897	1385
Co	4.1	5.5	34.4	38.5	1.6	0.4	11.9	17.9
Ni	27	46	536	803	5	4	76	175
Cu	2.55	7.17	1.02	1.31			7.73	14.31
Zn	22.1	21.0	22.5	12.0	18.3	12.4	19.9	18.3
As	0.48	2.06	0.22	0.17			0.25	0.33
Rb	0.06	0.05	0.09	0.10	0.24	0.33	0.03	0.03
Sr	12.60	12.90	9.37	8.92	6.94	5.81	5.56	10.87
Y	0.22	0.72	51.36	109.1	0.42	0.82	40.65	76.53
Zr	0.05		16.21	26.89	1.80	3.15	4.92	8.09
Nb	0.05		2.80	8.05	0.01	0.03	1.71	3.64
Mo	0.42	0.37	0.39	0.42	0.46	0.23	0.51	0.44
Ag			0.05					
Sn	0.89	0.31	1.43	1.50	0.85	0.27	3.55	7.99
Sb	0.21	0.22	0.19					
Ba	3.04	3.40	2.03	2.69	1.76	1.13	0.60	0.69
La	0.06	0.03	1.68	2.80	0.09	0.02	4.15	8.42
Ce	0.04	0.11	8.78	14.88	0.13	0.11	22.83	43.94
Pr	0.06	0.01	1.90	3.92	0.05	0.02	4.81	8.97
Nd	0.12	0.06	10.54	22.07	0.18	0.07	26.17	48.85
Sm	0.02	0.03	4.42	10.65	0.04	0.10	7.80	14.34
Eu	0.22	0.25	1.08	1.40	0.02	0.01	1.57	2.52
Gd	0.05	0.04	6.96	14.38	0.10		7.68	13.38
Tb	0.02	0.02	1.21	2.88	0.02		1.31	2.31
Dy	0.19	0.08	8.60	20.52	0.20	0.12	8.09	14.36
Ho	0.02	0.03	1.92	4.77	0.01		1.65	3.00
Er	0.14	0.14	6.01	14.78	0.16	0.20	4.42	9.15
Tm	0.03	0.03	0.94	2.35	0.03	0.02	0.59	1.34
Yb	0.13	0.21	6.52	16.31	0.08	0.09	3.49	7.68
Lu	0.04	0.06	0.97	2.36	0.01	0.02	0.47	0.90
Hf	0.12	0.06	1.06	1.52	0.14	0.12	0.07	0.17
Ta	0.00		0.25	0.39			0.10	0.24
Tl								
Pb	4.29	9.26	0.35	0.37	0.01			
Bi	0.00	0.01						
Th			0.04	0.05			0.06	0.11
U	0.00	0.00	0.00	0.01			0.01	0.02

^aTotal Fe as FeO. Blank stand for values below the limits of detection.

Serpentinized peridotites cut by hydrothermally altered magmatic veins						Amphibolitized oxide gabbro			
920D-16R-7, 19-22 (3)		920D-18R-3, 29-33 (5)		920D-18R-3, 48-54 (11)		920D-22R-5, 132-141 (2)		920D-12R-3, 96-98 (6)	
Mean	2σ	Mean	2σ	Mean	2σ	Mean	2σ	Mean	2σ
53.31	0.98	54.34	1.44	51.00	2.10	52.24	0.30	52.22	1.32
0.10	0.10	0.08	0.17	3.13	0.40	2.95	0.07	0.89	0.80
19.58	0.47	16.67	2.77	15.56	0.75	14.67	0.03	11.57	1.96
22.15	1.30	23.92	1.58	22.01	1.33	21.38	0.08	15.45	10.71
2.92	0.69	4.81	2.17	4.51	1.83	5.89	0.29	18.29	7.47
0.17	0.10	0.24	0.27	0.22	0.59	0.15	0.02	0.64	0.39
0.04	0.02	0.12	0.23	1.62	2.05	1.04	0.14	0.23	0.20
0.02	0.03	0.04	0.06	0.46	0.13	0.41	0.04	0.03	0.03
0.01	0.02	0.02	0.03	0.43	0.13	0.54	0.02	0.35	0.21
0.00	0.01	0.00	0.01	0.00	0.03	0.01	0.02	0.01	0.03
0.27	0.09	0.30	0.09	0.26	0.08	0.28	0.05	0.17	0.16
10.25	4.48	0.44		1.74	0.92	9.87	18.10	7.98	7.00
0.38	0.35	1.06		89.34	17.49	72.70	165.21	144.24	82.50
113.0	122.3	904.2		5625.0	1674.9	2430.0	3123.2	1949.0	828.3
2.44	0.19	267.53		432.81	76.65	205.85	380.66	78.46	68.54
162.7	17.0	190.3		2112.2	341.8	992.2	1607.0	16.6	28.9
872	657	2498		1220	913	1368	1258	4167	1645
18.1	1.9	27.2		22.7	13.0	75.6	98.0	46.0	14.6
388	12	101		194	57	461	485	143	45
0.37	0.10	44.69		7.05	18.31			2.68	9.21
17.2	4.1	64.0		19.1	6.1	40.2	13.3	169.4	71.7
				0.10	0.05			1.24	0.42
0.11	0.08	0.26		0.03	0.02	0.08	0.12	0.24	0.16
3.26	4.54	9.92		7.06	2.47	8.20	1.60	18.47	28.79
0.02	0.01	1.82		33.53	5.64	13.14	29.85	359.67	160.78
		0.06		59.17	12.97	9.83	24.77	249.69	124.31
0.07	0.08	0.10		0.13	0.10	0.02	0.02	0.05	0.04
0.38	0.30	0.80		0.46	0.30	0.24	0.04	1.72	0.89
				0.02	0.01			0.08	0.06
0.15	0.10	0.29		0.70	0.54	0.81	0.87	1.91	1.15
				0.03					
0.48	0.76	2.26		0.19	0.20	0.34	0.49	0.65	1.29
0.02	0.02	0.57		0.88	0.32	0.15		7.80	4.89
0.06	0.06	1.74		4.71	1.50	0.49	1.26	46.61	28.87
0.01	0.01	0.26		1.08	0.30	0.13	0.32	12.29	7.19
0.01	0.01	1.15		7.02	1.75	1.07	2.61	76.54	39.03
		0.24		3.28	0.61	0.75	1.90	35.19	14.94
0.08	0.10	0.22		0.96	0.18	0.28	0.73	4.67	1.59
0.01		0.18		4.90	0.82	1.33	3.31	49.58	20.66
		0.02		0.90	0.14	0.29	0.69	9.89	4.22
		0.19		6.14	0.87	2.20	4.99	65.38	31.58
		0.06		1.32	0.26	0.47	1.04	14.53	6.96
0.02		0.31		3.79	0.80	1.62	3.45	42.90	19.68
		0.07		0.50	0.10	0.25	0.51	6.35	3.39
		0.84		3.21	0.65	1.63	3.17	43.73	22.16
		0.12		0.46	0.10	0.27	0.46	6.55	3.18
				2.11	0.41	0.41	1.02	9.64	3.62
				0.01	0.01	0.00		0.01	0.02
				0.01				0.03	
0.01		0.11		0.13	0.15	0.35		0.14	0.09
				0.01	0.01			0.02	0.01
		0.06		0.02	0.01			0.06	0.08
		0.00		0.01	0.01			0.02	0.04

Table 5
Major and Trace Element Compositions of Amphibole in Mantle and Magmatic Rocks at Holes 920B and 920D of the Mid Atlantic Ridge Kane Area

Petrographic facies	Serpentinized peridotites cut by hydrothermally altered magmatic veins										Amphibolitized oxide gabbro	
	920B-4R-1, 76-77 (20)		920B-11R-1, 100-108 (31)		920D-17R-1, 46-48 (32)		920D-18R-3, 29-33 (18)		920D-22R-5, 131-135 (15)		920D-12R-3, 96-98 (20)	
	Sample (n)	Mean	2σ	Mean	2σ	Mean	2σ	Mean	2σ	Mean	2σ	Mean
Major element (wt. %)												
SiO ₂	53.28	4.35	54.06	5.09	51.69	10.01	52.25	4.30	55.93	4.95	50.16	4.42
Al ₂ O ₃	4.90	4.89	3.19	4.04	6.78	9.45	5.02	3.90	1.28	3.48	3.77	4.05
MgO	20.74	1.66	19.86	3.28	19.25	5.26	20.29	1.98	19.98	3.78	11.61	2.52
CaO	11.62	0.68	11.24	1.12	12.45	1.41	11.81	0.77	12.50	1.97	8.70	5.11
FeO ^a	4.72	0.90	6.72	4.31	4.88	5.02	5.35	1.66	6.41	4.35	21.18	5.22
MnO	0.12	0.11	0.11	0.10	0.06	0.09	0.08	0.07	0.29	0.24	0.53	0.45
TiO ₂	0.10	0.28	0.48	0.86	0.52	1.19	0.16	0.17	0.18	0.97	0.34	0.53
Cr ₂ O ₃	0.16	0.24	0.19	0.37	0.04	0.06	0.67	0.83	0.07	0.09	0.02	0.03
Na ₂ O	1.57	1.32	1.05	1.14	1.63	2.11	1.68	1.06	0.33	0.89	1.05	1.08
K ₂ O	0.05	0.04	0.04	0.09	0.05	0.06	0.04	0.03	0.02	0.05	0.08	0.10
P ₂ O ₅	0.14	0.10	0.12	0.07	0.14	0.07	0.14	0.08	0.15	0.07	0.10	0.07
Trace element (ppm)												
Li	0.32	0.31	1.11	2.08	0.53	0.99	0.54	0.35	3.60	6.49	0.20	0.15
Sc	20.97	14.21	29.00	61.68	7.56	23.12	30.01	19.80	20.51	36.63	33.75	41.52
Ti	63.6	62.7	2681.3	5829.1	1926.7	4378.8	907.5	357.1	930.7	2223.6	1838.6	2977.7
V	58.16	60.61	163.39	240.87	122.20	168.78	213.47	39.03	68.00	241.62	80.43	171.38
Cr	1049.2	1096.3	1058.9	1787.0	120.7	265.1	4197.9	2278.7	228.2	584.3	29.9	74.4
Mn	678	186	941	457	426	428	864	197	1483	1381	4076	2758
Co	27.3	6.9	46.4	47.2	37.4	30.2	38.5	5.7	47.9	43.7	54.7	15.5
Ni	608	297	741	803	1291	1552	618	81	539	497	176	97
Cu	1.44	0.61	2.43	3.88	3.16	6.01	1.91	0.53			4.08	11.20
Zn	12.7	5.2	17.8	10.6	11.2	11.4	18.6	6.0	38.5	22.5	230.8	96.7
As	0.41	0.36	0.39	0.50	0.29	0.49	0.24	0.10	0.11	0.00	0.33	0.23
Rb	0.04	0.03	0.11	0.16	0.05	0.04	0.05	0.01	0.07	0.07	0.10	0.10
Sr	6.18	1.65	10.71	10.20	10.96	10.00	8.64	1.72	13.11	11.64	10.44	10.87
Y	72.61	50.57	89.16	189.7	29.55	87.99	24.86	12.47	5.63	17.29	78.56	89.21
Zr	69.19	63.89	39.84	96.98	30.65	81.51	9.66	8.73	1.64	4.77	16.66	39.45
Nb	0.89	1.07	2.50	5.00	3.29	6.18	1.53	1.16	0.02	0.05	0.19	0.43
Mo	0.25	0.07	0.40	0.23	0.16	0.13	0.28	0.09	0.33	0.38	1.69	1.27
Ag	0.03	0.01	0.05									
Sn	1.63	0.91	2.56	5.69	1.40	2.73	2.04	0.89	0.87	0.99	1.49	1.96
Sb	0.03				0.03	0.01			0.10	0.04	0.02	
Ba	0.12	0.10	0.68	2.31	0.71	1.35	0.20	0.11	0.79	0.74	1.15	1.12
La	5.87	4.96	4.34	9.75	2.65	7.24	3.59	1.45	0.35	0.69	3.16	3.51
Ce	35.38	31.42	22.07	40.85	12.56	37.55	18.56	8.03	0.77	1.57	16.44	17.81
Pr	7.79	7.43	4.73	8.43	2.45	7.68	3.31	1.59	0.14	0.22	3.60	3.89
Nd	43.68	43.11	25.70	43.03	13.05	40.40	17.73	9.20	0.69	1.08	22.00	23.65
Sm	13.84	13.99	9.80	17.98	4.14	12.78	4.99	2.71	0.22	0.49	8.16	8.94
Eu	1.73	0.62	2.00	2.91	1.64	2.82	1.89	0.87	0.27	0.39	3.22	3.37
Gd	13.96	11.76	13.01	24.68	4.79	14.00	4.87	2.69	0.43	1.15	10.34	12.02
Tb	2.34	1.92	2.41	5.05	0.90	2.56	0.79	0.42	0.10	0.29	2.00	2.37
Dy	14.47	11.38	17.14	34.67	5.57	16.31	5.15	2.70	0.83	2.51	13.78	15.97
Ho	2.98	2.17	3.89	8.09	1.26	3.57	1.03	0.53	0.20	0.63	3.20	3.70
Er	8.63	6.24	11.38	25.21	3.58	10.31	2.95	1.42	0.77	2.05	10.18	10.80
Tm	1.25	0.90	1.78	4.05	0.50	1.48	0.43	0.20	0.15	0.36	1.61	1.65
Yb	8.22	5.53	12.71	28.46	3.53	10.62	2.97	1.39	1.08	2.60	12.00	11.71
Lu	1.16	0.74	1.94	4.05	0.48	1.44	0.45	0.20	0.18	0.37	1.94	1.84
Hf	4.14	2.96	1.84	4.68	2.09	5.10	0.27	0.23	0.09	0.18	0.58	1.43
Ta	0.05	0.08	0.18	0.35	0.33	0.77	0.04	0.02	0.00	0.00	0.02	0.04
Tl			0.01	0.01	0.01		0.02				0.01	0.00
Pb			0.07	0.16	0.12	0.27	0.03	0.01	0.16	0.27	0.07	0.14
Bi	0.00	0.00	0.00	0.00	0.00	0.00			0.01	0.01	0.01	0.01
Th	0.23	0.30	0.14	0.16	0.06	0.13	0.13	0.12			0.06	0.10
U	0.02	0.02	0.01	0.01	0.01	0.02	0.01	0.02	0.00	0.00	0.01	0.02

^aTotal Fe as FeO. Blank stand for values below the limits of detection.

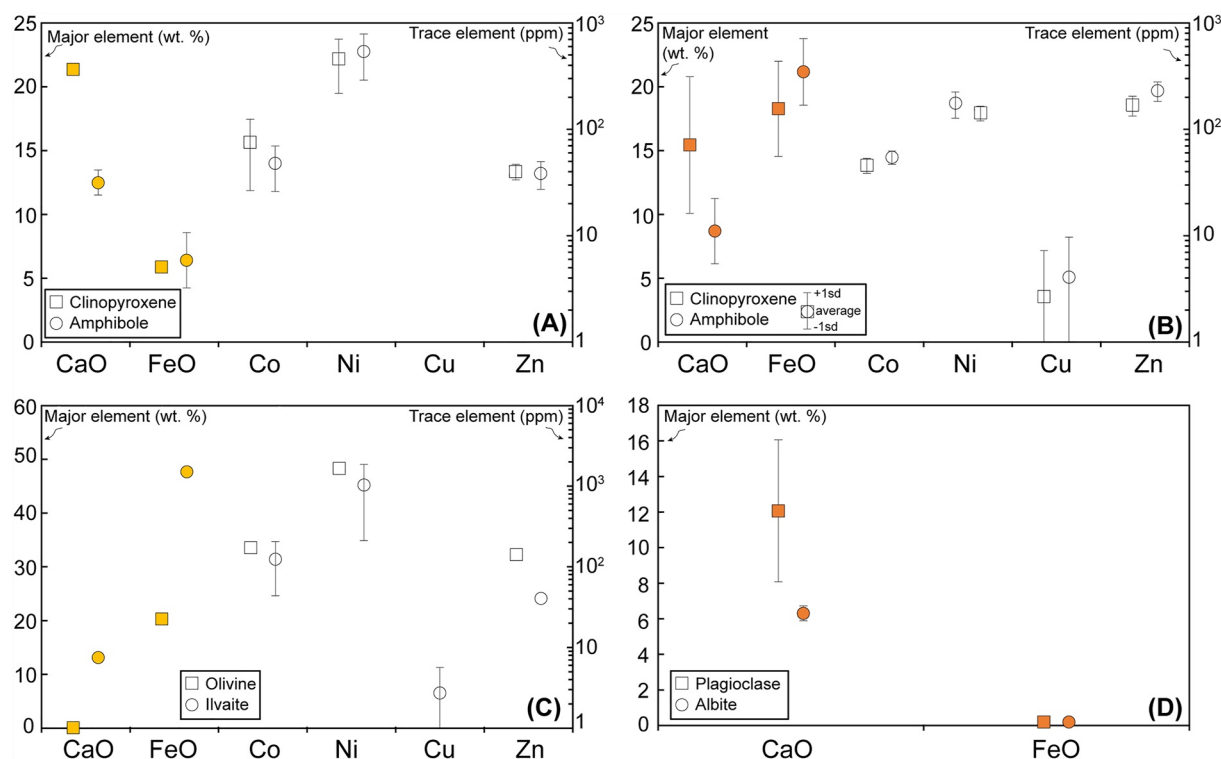


Figure 9. Mineral pairs element analyses for CaO, FeO, Co, Ni, Cu, and Zn during different mineralogical reactions. Amphibolitization of clinopyroxene in panel (a) hydrothermally altered magmatic vein (920D-22R-5, 132-141), (b) amphibolitized oxide gabbro (920D-12R-3, 96-100), (c) ilvaiteization of olivine, and (d) albitization of plagioclase. CaO and FeO contents of magmatic plagioclase in mafic intrusions of Site 920 are from Cannat et al. (1997). Other minerals are from this study. Full and empty symbols refer to as major and trace elements, respectively. Error contained in the symbol unless displayed.

otites of Site 920 (Figure 6, Figure S2 in Supporting Information S1, Burgath et al., 1997; Cannat et al., 1997; Stephens, 1997; Werner & Pilot, 1997).

Melt-rock interaction occurs at high temperatures (>825°C), during magma injection in the residual lithospheric mantle. Magmatic veins do not present evidence for ductile deformation, suggesting that mantle rocks have already passed the transition from asthenosphere to lithosphere at the time of magma injection (Casey, 1997). Olivine and orthopyroxene occur as primary mantle silicates and do not present textural evidence for recrystallization (e.g., olivine crystallizing after serpentine during heating). This indicates that magma channelizing and melt-rock interaction take place prior to serpentinization of peridotite, according to the presence of serpentine veins that cut through magmatic veins (Figure 2). Hence, magma channelizing and melt-rock interaction have to occur in a depth range narrowed between the base of the mechanical lithosphere and the zone of efficient serpentinization of the lithospheric mantle. This is further discussed below.

4.1.2. High Temperature Hydrothermal Fluid Circulation Overprint

Fluid circulation is attested by the formation of secondary hydrous (e.g., amphibole, ilvaite, hydro-andradite, chlorite, talc, and serpentine) and anhydrous phases (e.g., clinopyroxene) in the former mantle and magmatic rocks. At the contact between magmatic veins and peridotites, this leads to the formation of ilvaite (and hydro-andradite) at the expense of mantle silicates (Figures 3e–3g). This suggests spatial, and likely genetic, relationships between magmatic veining and Fe–Ca silicates formation.

Most clinopyroxene has low TiO_2 , Na_2O , Al_2O_3 , and Cr_2O_3 contents (Figures 7b and 7c), differing to the ones of mantle clinopyroxene of Site 920. Together with the low, even though variable, REE compositions of clinopyroxene (Figure S4 in Supporting Information S1), this points to a hydrothermal origin (Coltat et al., 2021, 2023). The measured variability of REE compositions of clinopyroxene (and amphibole) suggests complex fluid-rock interaction processes, a point discussed in the following section.

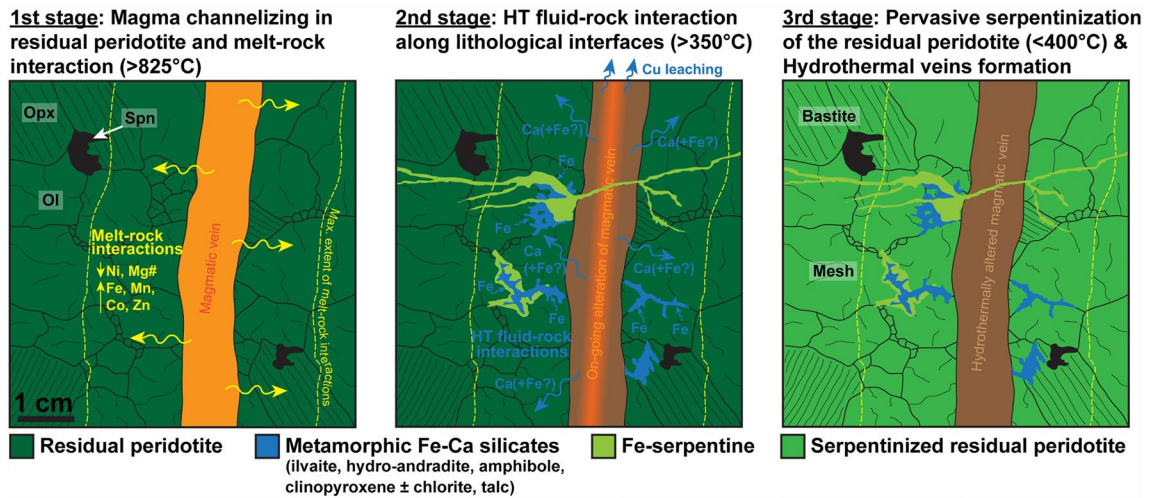


Figure 10. Schematic sketch showing melt-rock and subsequent fluid-rock interactions leading to Fe-Ca metasomatism and serpentinization of mantle rocks of Site 920. See text for details.

After petrographic evidence, Fe-Ca metasomatism occurs prior to the serpentinization of mantle rocks. Ilvaite directly replaces olivine in serpentinized peridotite at the contact with hydrothermally altered magmatic veins (Figure 3e), indicating that olivine serpentinization is not achieved before ilvaite formation. Ilvaite is stable together with hydro-andradite, clinopyroxene, amphibole, and Fe-antigorite, while lizardite was not observed. Antigorite is the HT polymorph of serpentine (Evans, 2004), and it may form after olivine at high temperatures (300°–600°C, Beard et al., 2009; Evans, 2010). This 300°–600°C temperature range overlaps the $425^\circ \pm 75^\circ\text{C}$ stability range of ilvaite-hydroandradite-clinopyroxene-magnetite mineral assemblages estimated by thermodynamic modeling (Gustafson, 1974). According to Coltat et al. (2023) we propose that Fe-Ca metasomatism results from fluid-rock interaction at temperatures between 350° and 600°C, high temperatures that inhibit serpentinization of olivine (Allen & Seyfried, 2003).

Finally, several petrographic and geochemical lines of evidence point to an early magmatic stage altered by the formation of hydrothermal Fe-Ca silicates at MARK. The latter either replace primary magmatic and mantle silicates or precipitate as vein-filling minerals from the fluid (i.e., newly formed phases). Serpentinized peridotites at the contact with magmatic veins are enriched in Fe during melt-rock interaction (first stage in Figure 10), allowing to stabilize secondary Fe-rich minerals such as ilvaite and hydro-andradite during subsequent hydrothermal alteration (Figures 3c–3e, second stage in Figure 10). The magmatic veins are altered to amphibole, secondary clinopyroxene, chlorite, talc ± serpentine. Part of the amphibole might be formed during deuteric alteration of magmatic veins, while the rest of the secondary minerals likely derive from seawater circulation. We suggest that Fe-Ca metasomatism occurs at depth before mantle exhumation at the seafloor, where seawater entrainment and pervasive serpentinization are enhanced. Continuous mantle unroofing and exhumation in a brittle regime at decreasing temperatures is responsible for thermal cracking, allowing extensive fluid circulation and serpentinization of the peridotite footwall, as well as formation of hydrothermal veins (Andreani et al., 2007; Dilek et al., 1997, third stage in Figure 10).

4.2. Continuous Fluid-Rock Interaction Recorded in Mantle Rocks

The mineralogical and geochemical variability observed in clinopyroxene and amphibole in mantle and magmatic rocks at MARK point to complex fluid-rock interaction processes. In hydrothermally altered magmatic veins, amphibole shows variable Al_2O_3 , Na_2O , TiO_2 , Cr_2O_3 , and REE compositions (Figures 7 and 8, Figure S4 in Supporting Information S1). This is unlikely to be solely explained by partition coefficient from the phases amphibole grows (e.g., Coogan et al., 2001; Gillis & Meyer, 2001) but reflects the petrogenesis conditions of amphibole crystallization.

Pargasitic to actinolitic amphibole occurs in hydrothermally altered magmatic veins and in the amphibolitized oxide gabbro (Figures 2c and 3d, Figure S1a in Supporting Information S1). Ti-pargasite is a common magmatic amphibole observed in the oceanic crust (e.g., Cortesogno et al., 2004; Currin et al., 2018; Zhang et al., 2021), while actinolite rather derives from hydrothermal conditions at lower temperatures. At first order, the Ti content of amphibole may be used to constrain the formation temperature of amphibole (Ernst & Liu, 1998; Liao et al., 2021). The geothermometer has to be applied to Ca-amphibole associated with Ti-rich phases (e.g., titanite, rutile, and ilmenite). These conditions are satisfied in the amphibolitized oxide gabbro and in hydrothermally altered magmatic veins where Fe-Ti oxide and titanite occur, respectively. Using the geothermometer of Liao et al. (2021), we calculated formation temperature ranges of 422°–670°C and 419°–831°C in the amphibolitized oxide gabbro and in one hydrothermally altered magmatic vein, respectively. Such high temperatures (e.g., 600°C) favor Si-Al substitution in amphibole (Howie et al., 1992), and may account for the elevated Al₂O₃ content measured in some grains. These temperature ranges are roughly comprised between the sub-solidus temperature of magmatic rocks (~825°C) and the temperature of incipient serpentinization (<400°C). This suggests petrogenesis conditions during amphibole crystallization from the magmato-hydrothermal transition to hydrothermal conditions at MARK.

The variable REE compositions of amphibole (and clinopyroxene, Figure S4 in Supporting Information S1) are unlikely to be explained by magmatic heterogeneity. It may reflect continuous metamorphic recrystallization of primary igneous grains and/or newly formation, at variable thermal regimes, during hydrothermalism (Cortesogno et al., 2000). The REE compositions of amphibole, mimicking those of clinopyroxene, are likely due to the replacement of magmatic and/or secondary clinopyroxene, similar to what is observed in gabbro at MARK (Coogan et al., 2001; Cortesogno et al., 2000; Gillis & Meyer, 2001). The local high REE compositions of clinopyroxene would correspond to magmatic grains preserved from extensive recrystallization or secondary grains formed at low F/R ratios. Amphibole and clinopyroxene having low REE compositions preferentially show positive Eu anomaly (Figure S4 in Supporting Information S1), suggesting mineral recrystallization during hydrothermal circulation. Indeed, REEs, except Eu because of its divalent behavior, are difficultly mobilizable in hydrothermal fluids (Klinkhammer et al., 1994). Hence, mineral recrystallization at increasing F/R ratios would lead to the decrease of REE compositions of secondary grains.

4.3. Chemical Mobilities During Fe-Ca Metasomatism

4.3.1. Sources of Fe and Ca

Fe-Ca metasomatism implies both an enrichment of Ca and Fe in mantle rocks. Fe is poorly mobilizable in hydrothermal fluids during fluid-rock interaction, and particularly serpentinization, in the oceanic lithosphere. This is supported by the roughly similar Fe element and isotope compositions of abyssal serpentinites and peridotites (e.g., Craddock et al., 2013; Debret et al., 2018). On the contrary, Fe is mobile in magmas that can efficiently carry Fe upon long distances and produce important Fe elemental and isotopic heterogeneity in the oceanic mantle through melt metasomatism (e.g., Poitrasson et al., 2013; Weyer & Ionov, 2007). Therefore, it seems reasonable to think that Fe enrichment in serpentinized peridotite at MARK is due to magmatic veining. This is supported by the Fe enrichment observed in mantle olivine (and orthopyroxene), which is not a hydrothermal alteration product, at the contact with hydrothermally altered magmatic veins. Melt impregnation in peridotite is unlikely to produce olivine with such a high FeO content (up to 32.5 wt.%), but Fe diffusion during magma percolation in peridotite (i.e., melt-rock interaction, first stage in Figure 10) is likely an efficient mechanism to produce Fe enrichment in the peridotite wall (Poitrasson et al., 2013). This would need to be tested using isotopic modeling (e.g., Dauphas et al., 2010; Teng et al., 2011). Iron enrichment in peridotite requests the percolation of Fe-rich melts to promote a local geochemical gradient to enhance Fe diffusion. At MARK, Fe-rich evolved melts such as those forming oxide gabbro may favor such Fe diffusion in mantle rocks. As the melt percolates through mantle rocks, Fe would diffuse toward the surrounding mantle silicates, tending to reach chemical equilibrium. This is supported by the high FeO content measured in serpentinized peridotite at the contact with magmatic veins at Kane (Ciazela et al., 2018). However, all magmatic veins at MARK certainly do not derive only from Fe-rich melts (Cannat et al., 1995). In some instances, the percolation of Fe-poor melts hampers Fe diffusion, explaining the variable FeO content of olivine in serpentinized peridotites at the contact with magmatic veins. The determination of the primary composition and nature of magmatic veins are obscured because of extensive

hydrothermal alteration. We cannot rule out that part of Fe derives from this hydrothermal event (second stage in Figure 10), even if we think that Fe diffusion during melt-rock interaction primarily controls the Fe budget.

Melt-rock interaction may have significant effect on Ca isotope compositions of mantle rocks (Kang et al., 2017), but has only limited effect on Ca element mobility. Indeed, Kang et al. (2017) reported CaO compositions for metasomatized xenolithic peridotites similar to those of un-metasomatized samples, suggesting little or no Ca enrichment in peridotite during metasomatism. This is likely due to the relative absence of major mantle silicates (i.e., olivine and orthopyroxene) that can incorporate Ca from the metasomatizing melt/fluid. Conversely, fluid-rock interaction can efficiently mobilize Ca from the oceanic lithosphere rocks, producing important isotopic and elemental heterogeneities (e.g., Amini et al., 2008; Cann & Gillis, 2004; Hu et al., 2023). More likely, calcium might either derive from hydrothermal alteration of Ca-bearing minerals in magmatic veins or the seawater-derived hydrothermal fluid itself. Ca isotope compositions of rodingite in the Leka ophiolite complex (Norway) indicate that Ca entirely derives from the breakdown of Ca-bearing mantle silicates without any component of Ca seawater (Gussone et al., 2020). This suggests that Ca primarily derives from the breakdown of Ca-bearing silicates. At MARK, secondary mineralogical reaction such as amphibolitization of clinopyroxene and albitization of plagioclase are responsible for Ca losses in altered magmatic rock (Figures 9a, 9b, and 9d). The volume of altered magmatic rocks at MARK is not constrained, but considering the low spatial extent where Fe-Ca metasomatism occurs in serpentinized peridotites at the contact with magmatic veins, those mineralogical reactions certainly significantly account for the Ca budget in Fe-Ca silicates (second stage in Figure 10).

4.3.2. Metal Mobilities

Metals (Ni, Co, Cu, and Zn) are mainly sourced in the different minerals constituting mantle and magmatic rocks, as the original fluid (e.g., seawater) contains very low metal contents (e.g., Charlou et al., 2002; Sohrin et al., 1998). Mantle olivine is the main source of Ni and Co, while Zn is primarily hosted in spinel (e.g., Guo et al., 1999; Z.-Z. Wang et al., 2017), and Cu in sulfides. Hence, metal mobility is directly dependent to the relative stability of these minerals with respect to metamorphic reactions.

Mantle rocks at MARK do not present systematic variations of their Co, Ni and Zn contents compared to abyssal serpentinized peridotites (Figures 4e, 4f, and 4h). This results from the competition between three processes: (a) Co and Zn enrichment and Ni depletion in mantle rocks through melt-rock interaction, (b) release of Ni, Co and Zn during ilvaization of olivine (Figure 9b), and (c) release of Zn during spinel breakdown. In our samples, the processes (a) and (b) only very locally influence the chemical composition of the rock. This is likely not captured by bulk rock chemistry. The lack of apparent variation of the Zn content of the studied samples implies the stability of spinel during Fe-Ca metasomatism.

On the other hand, the amphibolitized oxide gabbro and serpentinized peridotites cut by hydrothermally altered magmatic veins are depleted in Cu with respect to mafic intrusions and abyssal serpentinized peridotites, respectively (Figure 4g). This apparent Cu depletion cannot be simply explained in terms of mixing between two peridotite and magmatic (gabbro or pyroxenite) poles, as gabbro and pyroxenite are enriched in Cu compared to peridotite (e.g., Casey, 1997; Frey, 1980; Garrido & Bodinier, 1999; Sossi et al., 2018; Tilhac et al., 2016). Magmatic veining in peridotite would increase the Cu content of the rock. Primary sulfides were neither observed in magmatic veins nor in the amphibolitized oxide gabbro. Therefore, the Cu depletion is likely the consequence of the dissolution of the mantle and magmatic sulfides during HT (>350°C) hydrothermal alteration (second stage in Figure 10), in good agreement with previous studies (e.g., Patten et al., 2016).

4.4. Tectono-Hydrothermal Model for Fe-Ca Metasomatism

Metamorphic mineral reactions at MARK occurred over a broad range of temperature, from ~830° to <300°C, based on mineralogical and geochemical indicators. The Fe-Ca metasomatism and formation of ilvaite, hydro-andradite, amphibole and clinopyroxene may further constrain this thermal range to 350°–600°C (see Section 4.1, Boschi et al., 2006; Dilek et al., 1997; Gustafson, 1974). The differences in temperature ranges may provide an indication of plausible subseafloor depths, based on thermal gradients, and a lithospheric setting based on the seismic velocity structure.

The seismic velocity of the axial lithosphere is mainly controlled by composition (peridotite, serpentinite, gabbro), cracking, and the presence of molten material (below the rift valley floor). Steep velocity gradients

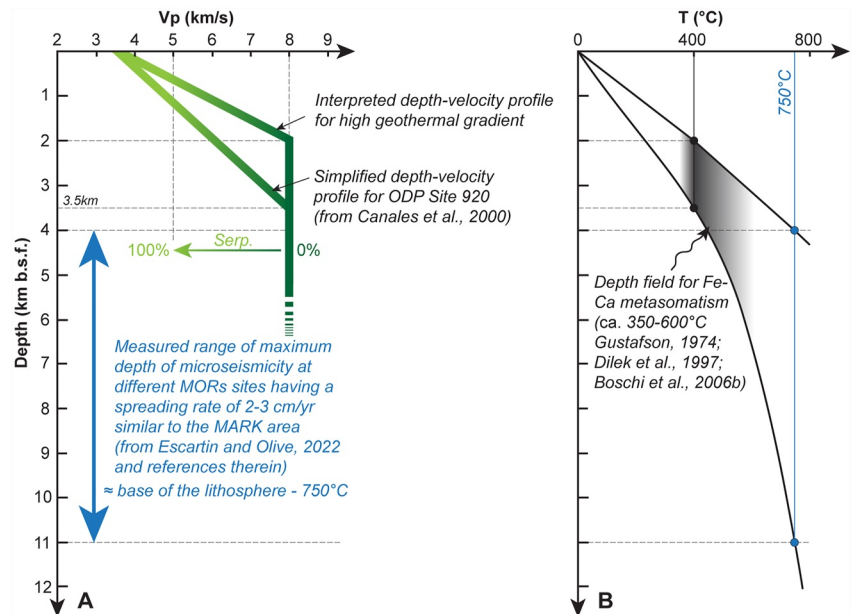


Figure 11. (a) Modified depth-velocity profile for the site 920 at Mid Atlantic Ridge Kane (MARK) (from Canales et al. (2000)) and interpreted depth velocity-profile considering high geothermal gradient. The depth range of maximum micro-seismicity at Mid-Oceanic Ridge sites having a similar spreading rate than the MARK area is also displayed (after Escartín and Olive (2022)). (b) Interpreted geothermal gradient curves and depth field for Fe-Ca metasomatism.

in the shallow subseafloor in lithosphere outcropping peridotites, such as the MARK area, are interpreted as a combination of both fracture closure and decrease in the degree of serpentinization, reaching mantle velocities at depths from ~2 to ~3.5 km (Canales et al., 2000). Serpentinization in oceanic mantle rocks is dominated by lizardite and chrysotile forming at temperatures <400°C, in the presence of water (Evans, 2004). At higher temperatures, antigorite is formed instead (Evans, 2004; Moody, 1976), and generally does not result in pervasive replacement (Viti & Mellini, 1998).

At Site 920, early serpentinization was estimated to have occurred at $T > 350^{\circ}\text{C}$ after O isotope analysis (Agrinier & Cannat, 1997), while Alt and Shanks (2003) proposed that peridotite hydration occurred at a maximum temperature of 400°C after sulfur mineralogy, content and isotopes. A similar serpentinization temperature value was advanced by Rouméjon and Cannat (2014) for the MARK area. Assuming that the temperature limit for oceanic serpentinization is ~400°C, the simplified seismic profiles provide a possible range of temperature gradients, as shown in Figure 11b.

Hydrothermal circulation requires fluid paths and hence a brittle lithosphere, that may reach temperatures of up to ~750°C (e.g., Escartín & Olive, 2022). Microseismicity has been used as a proxy to estimate this brittle thickness, as indicated by the maximum depth of the seismic activity. At MOR sections with comparable spreading rates (e.g., ~2–3, ~2.5 cm/yr at the MARK area), the maximum depth of seismic studies ranges between 4 and 11 km below seafloor (DeMartin et al., 2007; Grevemeyer et al., 2013; Horning et al., 2018; Parnell-Turner et al., 2017; Tilmann et al., 2004; Wolfe et al., 1995; see Escartín & Olive, 2022 for a review); this range in depth of seismicity is shown in Figure 11a, and used to constrain the range of thermal gradients in Figure 11b to temperatures of ~750°C. Considering the thermal gradients in Figure 11b and the temperatures between 350° and 600°C for Fe-Ca metasomatism, we propose that this results from fluid circulations at depths that may range from ~2 to ~6.5 km below seafloor. However, the upper limit may not be plausible since pervasive serpentinization may be achieved at such shallow depths. The lower limit is consistent with the depth estimated for initial detachment faulting at slow-spreading ridges (DeMartin et al., 2007; Grevemeyer et al., 2013) and suggests that fluid circulation started during incipient mantle exhumation rather than late mantle denudation and unroofing.

4.5. Present-Day Setting of Fe-Ca Metasomatism and Implications for the Formation of Seafloor Massive Sulfide Deposits

Several models of fluid circulation associated with detachment faults exist in the literature, with HT fluid circulation that may operate (a) along detachment fault zones exhuming deep mantle rocks, either with a link to surface discharge (e.g., DeMartin et al., 2007; McCaig et al., 2010), or with fluids interacting along the fault only at depth and not linked to surface hydrothermalism (e.g., Bonnemains et al., 2017; Verlaquet et al., 2021); or (b) circulating within the footwall of a core complex with outflow at the seafloor, such as the Rainbow massif (Andreani et al., 2014) or the detachments in the 13°N area along the MAR (Escartin et al., 2017). In both scenarios (Figures 12a and 12b), fluid circulation may be facilitated by fault-assisted permeability (detachment fault, late faults cross-cutting the exposed core complex) but there are different timings for associated Fe-Ca metasomatism in mantle rocks. In first model, with fluid circulation along the permeable detachment fault zone, Fe-Ca metasomatism could operate early at the base of the detachment fault, and prior to extensive serpentinization of the peridotite basement (Figure 12a). In the second model, mantle rocks uplifted by the detachment may be preserved from extensive serpentinization during exhumation, consistent with high seismic velocity and thin crust associated with these structures (Blackman et al., 2009). Subsequent deformation and magmatic emplacement within the footwall may provide both heat sources and fluid paths for hydrothermal circulation accessing fresh mantle rocks (Figure 12b). This type of late off-axis magmatic injection into pristine mantle rocks is consistent with petrographic observations in the MARK area of Fe-Ca metasomatism in pristine peridotite.

Fe-Ca metasomatism is unlikely to occur in more magmatically robust ridge sections, with a well-developed oceanic crust without exhumation of mantle rocks at the seafloor. In these environments, mantle rocks are likely to be deep-seated (>4–5 km below seafloor), where seawater circulation may be generally restricted to the upper magmatic portion of the oceanic lithosphere without reaching the upper mantle (e.g., Alt, 1995; Schwarzenbach & Steele-MacInnis, 2020).

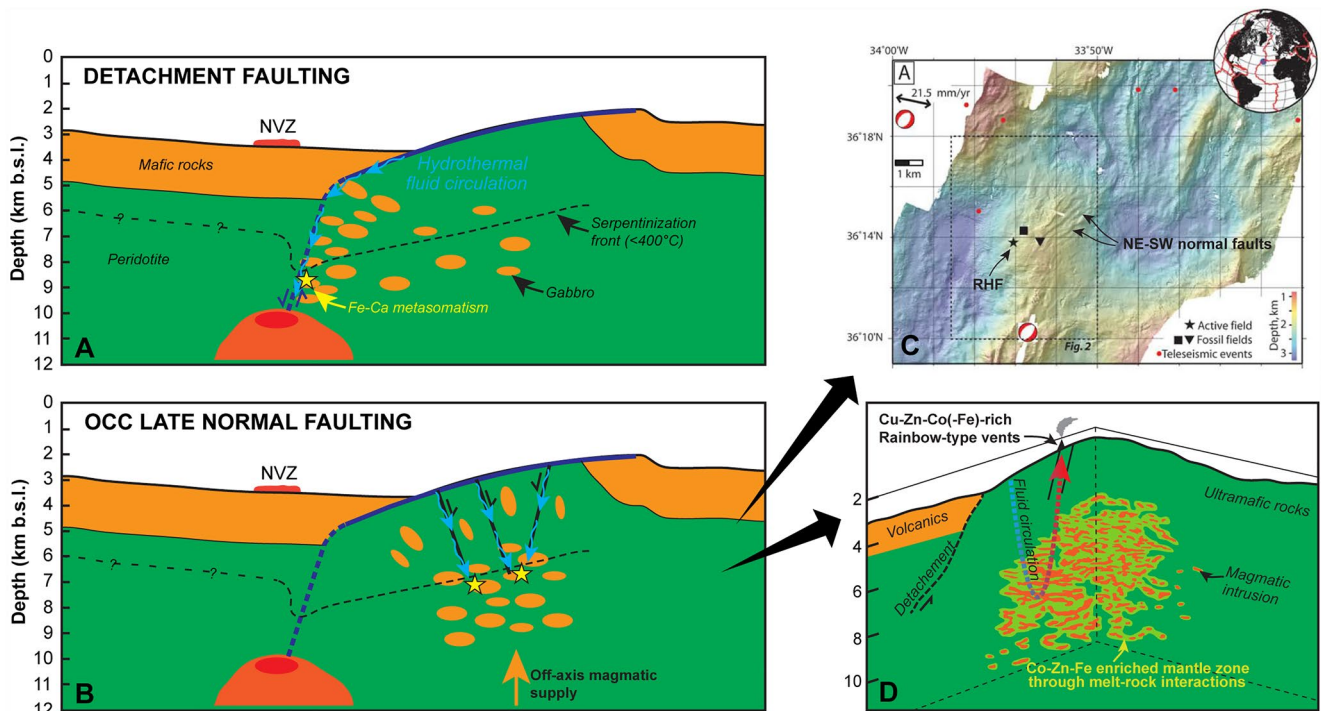


Figure 12. Schematic tectono-magmatic sketches showing possible zones where Fe-Ca metasomatism may occur at MORs (yellow star) after melt-peridotite interactions in the context of (a) mantle exhumation along a detachment fault and (b) late normal faulting of an oceanic core complex (modified from DeMartin et al. (2007)). (c) Bathymetric map of the Rainbow massif showing the location of the Rainbow hydrothermal field (RHF). (d) Schematic cartoon showing High Temperature fluid circulations below the RHF. Fluid pathways are speculative as the root depth of normal faults cutting through the massif is not known. Note the control of melt-rock interactions on the metal endowment in the mineralization (modified from Andreani et al. (2014) and Canales et al. (2017)). See text for details.

The Fe-Ca metasomatism that we document is likely limited volumetrically, at the scale of a detachment fault. Metasomatic zones show thicknesses of a few millimeters to centimeters around magmatic dykelets. Furthermore, the proportion of mafic intrusions at site 920 is less than 4% of recovered rocks at Holes 920B and 920D (Cannat et al., 1997). This suggests that Fe-Ca metasomatism and related alteration do not significantly impact the physical and chemical properties of the host rock at the scale of the detachment footwall. This volumetric proportion may increase in other systems with more significant magmatic supply into pristine mantle lithosphere. Indeed, the extent of metal enrichment in mantle rocks seems to be linked to the size of magmatic intrusions (e.g., Cannat et al., 1997; Coltat et al., 2023; Niida, 1997). Hence, large magmatic intrusions in peridotite may be associated with important volumes of mantle rocks enriched in Fe, Co, and Zn. If the descending hydrothermal fluid may react with magmatic and enriched mantle rocks, leaching and transporting metals (Fe, Co, Cu, Zn), it would eventually promote SMS formation. The above statement comes true only if (a) magmatic rocks incept in a fresh peridotite basement, providing heat and chemical exchanges and (b) fault-controlled permeable zones allow vertical fluid flow to these zones.

At the Rainbow massif (36°N, MAR), a network of normal faults crosscuts the massif and allows vertical fluid circulation (Figure 12c, Andreani et al., 2014). Deep magmatic lenses (>2 km below seafloor) have been imaged by seismic studies below the active field (Figure 12d, Canales et al., 2017), and are thought to have incept in a fresh peridotite basement. Anomalous high Fe, Co, and Zn contents have been measured in the Rainbow venting fluid (Charlou et al., 2002; Douville et al., 2002), being one to two orders of magnitude higher than in other SMS-related hydrothermal fluids, suggesting that fluid-enriched mantle rock interactions occur in the basement of the Rainbow massif (Figure 12d). The elevated Cu content of the mineralizations at Rainbow might be ascribed to fluid-magmatic rocks interaction, dissolving magmatic sulfides and oxides during HT hydrothermal alteration, as observed at MARK (Figure 4g). Hence, we propose that the coupling between melt-rock and fluid-rock interactions in a heterogeneous oceanic lithosphere is certainly a suitable candidate to explain the variable metal enrichments recorded in UM-SMS. It might likely be extrapolated to systems where permeable fault zone and magmatic inception allow HT (>350°C) fluid circulation in the exposed mantle rocks (e.g., the Irinovskoe, Semenov and Ashadze hydrothermal fields at 13°N or the Logatchev hydrothermal field at 14°45'N). There, important volumes of magmatic bodies intruding mantle rocks have been inferred (e.g., Kelemen et al., 2007), likely producing important volumes of enriched mantle rocks.

5. Conclusions

Mantle rocks drilled during ODP Leg 153 at the MARK area recorded complex magmatic and hydrothermal processes during mantle exhumation. A combined petrographic and geochemical tracing on primary magmatic and secondary hydrothermal mineral assemblages allow to document an evolution for the MARK area ranging from (a) magma channelizing through the mantle and melt-rock interaction that leads to metal enrichment in the surrounding peridotite likely during incipient mantle exhumation, (b) subsequent fluid circulation along lithological interfaces that produces (Fe-)Ca mineral assemblages at temperatures between ~350° and 830°C and (c) late serpentinization of mantle rocks during progressive mantle denudation and unroofing at lower temperatures.

Complex magmato-hydrothermal processes account for important chemical mobilities in the mantle rocks (and likely in mafic rocks) of Site 920. Mantle rocks are notably enriched in Fe, Zn, and Co during melt-rock interaction, while HT fluid circulations (>350°C) are locally able to extract Cu from the magmatic rocks. However, because of the limited extent of hydrothermal alteration underwent by mantle and magmatic rocks at the MARK area, metal mobilities are likely limited. Nevertheless, we propose that these processes may have strong implications on the formation of ultramafic-hosted SMS at oceanic core complexes where hydrothermal fluids can percolate through the exhumed deep lithospheric rocks. Their coupling is likely a key factor to produce the variable metal enrichments reported at present-day hydrothermal SMS.

Data Availability Statement

All geochemical data obtained in this study supporting the results and interpretations of the manuscript are either available in figures, tables, or in Supporting Information S1. Data can be downloaded in free access at Open Science Framework (Coltat, 2023).

Acknowledgments

This work was funded through IODP-France (OPE-2021-93) and CNRS-INSU Grants to R. Coltat and J. Escartin. Analyses by LA-ICPMS at LERA are supported by the DFG fund INST121384/213-1 FUGG to C. Patten.

References

- Agrinier, P., & Cannat, M. (1997). Oxygen-isotope constraints on serpentinization processes in ultramafic rocks from the Mid-Atlantic Ridge (23°N). *Proceedings of the Ocean Drilling Program, Scientific Results*, 153, 381–388. <https://doi.org/10.2973/odp.proc.sr.153.033.1997>
- Allen, D. E., & Seyfried, W. E., Jr. (2003). Compositional controls on vent fluids from ultramafic-hosted hydrothermal systems at mid-ocean ridges: An experimental study at 400°C, 500 bars. *Geochimica et Cosmochimica Acta*, 67(8), 1531–1542. [https://doi.org/10.1016/S0016-7037\(02\)01173-0](https://doi.org/10.1016/S0016-7037(02)01173-0)
- Alt, J. C. (1995). Seafloor processes in mid-ocean ridge hydrothermal systems. *Geophysical Monograph-American Geophysical Union*, 91, 85.
- Alt, J. C., & Shanks, W. C. (2003). Serpentinization of abyssal peridotites from the MARK area, Mid-Atlantic Ridge: Sulfur geochemistry and reaction modeling. *Geochimica et Cosmochimica Acta*, 67(4), 641–653. [https://doi.org/10.1016/s0016-7037\(02\)01142-0](https://doi.org/10.1016/s0016-7037(02)01142-0)
- Amini, M., Eisenhauer, A., Böhm, F., Fietzke, J., Bach, W., Garbe-Schönberg, D., et al. (2008). Calcium isotope ($\delta^{44}\text{Ca}$) fractionation along hydrothermal pathways, Logatchev field (Mid-Atlantic Ridge, 14°45'N). *Geochimica et Cosmochimica Acta*, 72(16), 4107–4122. <https://doi.org/10.1016/j.gca.2008.05.055>
- Andreani, M., Escartin, J., Delacour, A., Ildefonse, B., Godard, M., Dymont, J., et al. (2014). Tectonic structure, lithology, and hydrothermal signature of the Rainbow massif (Mid-Atlantic Ridge 36°14'N). *Geochemistry, Geophysics, Geosystems*, 15(9), 3543–3571. <https://doi.org/10.1002/2014GC005269>. Received
- Andreani, M., Mével, C., Boullier, A.-M., & Escartin, J. (2007). Dynamic control on serpentine crystallization in veins: Constraints on hydration processes in oceanic peridotites. *Geochemistry, Geophysics, Geosystems*, 8(2), 24. <https://doi.org/10.1029/2006GC001373>
- Barrie, C. T., & Hannington, M. D. (1999). Classification of volcanic-associated massive sulfide deposits based on host-rock composition. In *Volcanic associated massive sulfide deposits: Processes and examples in modern and ancient settings*. Society of Economic Geologists.
- Beard, J. S., Frost, B. R., Fryer, P., McCaig, A., Searle, R., Ildefonse, B., et al. (2009). Onset and progression of serpentinization and magnetite formation in olivine-rich troctolite from IODP hole U1309D. *Journal of Petrology*, 50(3), 387–403. <https://doi.org/10.1093/ptrology/egp004>
- Beltenev, V., Ivanov, V., Rozhdestvenskaya, I., Cherkashov, G., Stepanova, T., Shilov, V., et al. (2007). A new hydrothermal field at 13 30' N on the Mid-Atlantic Ridge. *InterRidge News*, 16, 10.
- Blackman, D. K., Canales, J. P., & Harding, A. (2009). Geophysical signatures of oceanic core complexes. *Geophysical Journal International*, 178(2), 593–613. <https://doi.org/10.1111/j.1365-246X.2009.04184.x>
- Bonnemains, D., Escartin, J., Mével, C., Andreani, M., & Verlaquet, A. (2017). Pervasive silicification and hanging wall overplating along the 13°20'N oceanic detachment fault (Mid-Atlantic Ridge). *Geochemistry, Geophysics, Geosystems*, 18(6), 2028–2053. <https://doi.org/10.1002/2017GC006846>. Received
- Boschi, C., Früh-green, G. L., & Escartin, J. (2006). Occurrence and significance of serpentinite-hosted, talc-rich fault rocks in modern oceanic settings and ophiolite complexes. *Ophioliti*, 31, 129–140.
- Burgath, K.-P., Marchig, V., & Mussallam, K. (1997). 29. Data report: Mineralogic, structural, and chemical variability of mantle sections from Holes 920B and 920D. In *Proc. ODP. Sci. Results College Station, Texas* (Vol. 153).
- Canales, J. P., Collins, J. A., Escartin, J., & Detrick, R. S. (2000). Seismic structure across the rift valley of the Mid-Atlantic Ridge at 23 20'(MARK area): Implications for crustal accretion processes at slow spreading ridges. *Journal of Geophysical Research*, 105(B12), 28411–28425. <https://doi.org/10.1029/2000jb900301>
- Canales, J. P., Dunn, R. A., Arai, R., & Sohn, R. A. (2017). Seismic imaging of magma sills beneath an ultramafic-hosted hydrothermal system. *Geology*, 45(5), 451–454. <https://doi.org/10.1130/G38795.1>
- Cann, J., & Gillis, K. (2004). Hydrothermal insights from the Troodos ophiolite, Cyprus. In *Hydrogeology of the oceanic lithosphere* (pp. 274–311).
- Cannat, M., Chatin, F., Whitechurch, H., & Ceuleneer, G. (1997). 11. Gabbroic rocks trapped in the upper mantle at the Mid-Atlantic Ridge. In *Proc. Ocean drill. Program Sci. Results* (pp. 243–264).
- Cannat, M., Karson, J. A., Miller, D. J., & Party, S. S. (1995). ODP Leg 153 MARK initial report. In *Proceedings ODP. Initial Reports* (Vol. 153).
- Cannat, M., Karson, J. A., Miller, J., Agar, S., Barling, J., Casey, J., et al. (1994). Ocean drilling program, Leg 153 preliminary report on the Mid-Atlantic Ridge.
- Carbonin, S., Martin, S., Tumiati, S., & Rossetti, P. (2015). Magnetite from the Cogne serpentinites (Piemonte ophiolite nappe, Italy). Insights into seafloor fluid–rock interaction. *European Journal of Mineralogy*, 27(1), 31–50. <https://doi.org/10.1127/ejm/2014/0026-2410>
- Casey, J. F. (1997). Comparison of major- and trace-element geochemistry of abyssal peridotites and mafic plutonic rocks with basalts from the MARK region of the Mid-Atlantic Ridge. Scientific Results. In *Proceedings of the ocean drilling program* (pp. 181–241).
- Charlou, J. L., Donval, J. P., Fouquet, Y., Jean-baptiste, P., & Holm, N. (2002). Geochemistry of high H₂ and CH₄ vent fluids issuing from ultramafic rocks at the rainbow hydrothermal field (36°14'N, MAR). *Chemical Geology*, 191(4), 345–359. [https://doi.org/10.1016/S0009-2541\(02\)00134-1](https://doi.org/10.1016/S0009-2541(02)00134-1)
- Cherkashev, G. A., Ivanov, V. N., Bel'Tenev, V. I., Lazareva, L. I., Rozhdestvenskaya, I. I., Samovarov, M. L., et al. (2013). Massive sulfide ores of the northern equatorial Mid-Atlantic Ridge. *Oceanology*, 53(5), 607–619. <https://doi.org/10.1134/S0001437013050032>
- Cherkashov, G., Bel'tenev, V., Ivanov, V., Lazareva, L., Samovarov, M., Shilov, V., et al. (2008). Two new hydrothermal fields at the Mid-Atlantic Ridge. *Marine Georesources & Geotechnology*, 26(4), 308–316. <https://doi.org/10.1080/10641190802400708>
- Cherkashov, G., Poroshina, I., Stepanova, T., Ivanov, V., Bel'Tenev, V., Lazareva, L., et al. (2010). Seafloor massive sulfides from the northern equatorial Mid-Atlantic Ridge: New discoveries and perspectives. *Marine Georesources & Geotechnology*, 28(3), 222–239. <https://doi.org/10.1080/1064119x.2010.483308>
- Ciazela, J., Koepke, J., Dick, H. J. B., Botcharnikov, R., Muszynski, A., Lazarov, M., et al. (2018). Sulfide enrichment at an oceanic crust-mantle transition zone: Kane Megamullion (23°N, MAR). *Geochimica et Cosmochimica Acta*, 230, 155–189. <https://doi.org/10.1016/j.gca.2018.03.027>
- Coltat, R. (2023). Origin of Fe-Ca-metasomatism in exhumed mantle rocks at the MARK area (23°N, ODP Leg 153) and implications on the formation of ultramafic-hosted seafloor massive sulfide deposits [Dataset]. <https://doi.org/10.17605/OSF.IO/UQHTP>
- Coltat, R., Boulvais, P., Riegler, T., Pelleter, E., & Branquet, Y. (2021). Element distribution in the root zone of ultramafic-hosted black smoker-like systems: Constraints from an Alpine analog. *Chemical Geology*, 559, 119916. <https://doi.org/10.1016/j.chemgeo.2020.119916>
- Coltat, R., Branquet, Y., Gautier, P., Campos Rodriguez, H., Poujol, M., Pelleter, E., et al. (2019). Unravelling the root zone of ultramafic-hosted black smokers-like hydrothermalism from an Alpine analog. *Terra Nova*, 31(6), 549–561. <https://doi.org/10.1111/ter.12427>
- Coltat, R., Patten, C., Hochscheid, F., Branquet, Y., Ulrich, M., & Boulvais, P. (2023). On the origin of Fe-Ca metasomatism in ultramafic-hosted hydrothermal mineralized systems: Insights from the Platta Nappe (Swiss Alps). <https://doi.org/10.2139/ssrn.4480995>
- Coogan, L. A., Wilson, R. N., Gillis, K. M., & MacLeod, C. J. (2001). Near-solidus evolution of oceanic gabbros: Insights from amphibole geochemistry. *Geochimica et Cosmochimica Acta*, 65(23), 4339–4357. [https://doi.org/10.1016/S0016-7037\(01\)00714-1](https://doi.org/10.1016/S0016-7037(01)00714-1)

- Cortesogno, L., Gaggero, L., & Zanetti, A. (2000). Rare earth and trace elements in igneous and high-temperature metamorphic minerals of oceanic gabbros (MARK area, Mid-Atlantic Ridge). *Contributions to Mineralogy and Petrology*, 139(4), 373–393. <https://doi.org/10.1007/s004100000147>
- Cortesogno, L., Gaggero, L., & Zanetti, A. (2004). Rare earth and trace elements in amphiboles of oceanic gabbros (mark area, mid-Atlantic ridge) at medium-to low-temperature seafloor alteration. *Ophioliti*, 29, 107–123. <https://doi.org/10.4454/ofioliti.v29i2.209>
- Craddock, P. R., Warren, J. M., & Dauphas, N. (2013). Abyssal peridotites reveal the near-chondritic Fe isotopic composition of the Earth. *Earth and Planetary Science Letters*, 365, 63–76. <https://doi.org/10.1016/j.epsl.2013.01.011>
- Curran, A., Wolff, P. E., Koepke, J., Almeev, R. R., Zhang, C., Zihlmann, B., et al. (2018). Chlorine-rich amphibole in deep layered gabbros as evidence for brine/rock interaction in the lower oceanic crust: A case study from the Wadi Wariyah, Samail ophiolite, sultanate of Oman. *Lithos*, 323, 125–136. <https://doi.org/10.1016/j.lithos.2018.09.015>
- Dauphas, N., Teng, F.-Z., & Arndt, N. T. (2010). Magnesium and iron isotopes in 2.7 Ga Alexo komatiites: Mantle signatures, no evidence for Soret diffusion, and identification of diffusive transport in zoned olivine. *Geochimica et Cosmochimica Acta*, 74(11), 3274–3291. <https://doi.org/10.1016/j.gca.2010.02.031>
- Debret, B., Andreani, M., Delacour, A., Rouméjon, S., Trcera, N., & Williams, H. (2017). Assessing sulfur redox state and distribution in abyssal serpentinites using XANES spectroscopy. *Earth and Planetary Science Letters*, 466, 1–11. <https://doi.org/10.1016/j.epsl.2017.02.029>
- Debret, B., Beunon, H., Mattielli, N., Andreani, M., Ribeiro da Costa, I., & Escartín, J. (2018). Ore component mobility, transport and mineralization at mid-oceanic ridges: A stable isotopes (Zn, Cu and Fe) study of the rainbow massif (Mid-Atlantic Ridge 36°14'N). *Earth and Planetary Science Letters*, 503, 170–180. <https://doi.org/10.1016/j.epsl.2018.09.009>
- Delacour, A., Früh-green, G. L., & Bernasconi, S. M. (2008). Sulfur mineralogy and geochemistry of serpentinites and gabbros of the Atlantis Massif (IODP Site U1309). *Geochimica et Cosmochimica Acta*, 72(20), 5111–5127. <https://doi.org/10.1016/j.gca.2008.07.018>
- Demartin, B. J., Sohn, R. A., Canales, J. P., & Humphris, S. E. (2007). Kinematics and geometry of active detachment faulting beneath the Trans-Atlantic Geotraverse (TAG) hydrothermal field on the Mid-Atlantic Ridge. *Geology*, 35(8), 711–714. <https://doi.org/10.1130/g23718a.1>
- Detrick, R. S., Fox, P. J., Schulz, N., Pockalny, R., Kong, L., Mayer, L., & Ryan, W. B. F. (1988). Geologic and tectonic setting at MARK. In *Proceedings. Ocean Drilling Program, Mt. Repts.(PartA)* (Vol. 106, pp. 15–22).
- Dick, H. J. B., Johan Lissenberg, C., & Warren, J. M. (2010). Mantle melting, melt transport, and delivery beneath a slow-spreading ridge: The paleo-MAR from 23°15'N to 23°45'N. *Journal of Petrology*, 51(1–2), 425–467. <https://doi.org/10.1093/petrology/egp088>
- Dick, H. J. B., Tivey, M. A., & Tucholke, B. E. (2008). Plutonic foundation of a slow-spreading ridge segment: Oceanic core complex at Kane Megamullion, 23°30'N, 45°20'W. *Geochemistry, Geophysics, Geosystems*, 9(5), Q05014. <https://doi.org/10.1029/2007GC001645>
- Dilek, Y., Coulton, A., & Hurst, S. D. (1997). Serpentinization and hydrothermal veining in peridotites at site 920 in the Mark area. In *Proceedings-Ocean drilling program scientific results* (pp. 35–60). National Science Foundation.
- Ding, T., Tao, C., Dias, Á. A., Liang, J., Chen, J., Wu, B., et al. (2020). Sulfur isotopic compositions of sulfides along the southwest Indian ridge: Implications for mineralization in ultramafic rocks. *Mineralium Deposita*, 1–16. <https://doi.org/10.1007/s00126-020-01025-0>
- Douville, E., Charlou, J. L., Oelkers, E. H., Bienuvenu, P., Jove Colon, C. F., Donval, J., et al. (2002). The rainbow vent fluids (36°14'N, MAR): The influence of ultramafic rocks and phase separation on trace metal content in Mid-Atlantic Ridge hydrothermal fluids. *Chemical Geology*, 184(1–2), 37–48. [https://doi.org/10.1016/s0009-2541\(01\)00351-5](https://doi.org/10.1016/s0009-2541(01)00351-5)
- Ernst, W. G., & Liu, J. (1998). Experimental phase-equilibrium study of Al- and Ti-contents of calcic amphibole in MORB—A semiquantitative thermobarometer. *American Mineralogist*, 83(9–10), 952–969. <https://doi.org/10.2138/am-1998-9-1004>
- Escartín, J., Mével, C., Petersen, S., Bonnemaïn, D., Cannat, M., Andreani, M., et al. (2017). Tectonic structure, evolution, and the nature of oceanic core complexes and their detachment fault zones (13°20'N and 13°30'N, Mid Atlantic Ridge). *Geochemistry, Geophysics, Geosystems*, 18(4), 1451–1482. <https://doi.org/10.1002/2016GC006775>
- Escartín, J., & Olive, J. A. (2022). Mid-Ocean ridges and their geomorphological features. *Journal: Treatise on Geomorphology*, 847–881. <https://doi.org/10.1016/B978-0-12-818234-5.00193-0>
- Evans, B. W. (2004). The serpentinite multisystem revisited: Chrysotile is metastable. *International Geology Review*, 46(6), 479–506. <https://doi.org/10.2747/0020-6814.46.6.479>
- Evans, B. W. (2010). Lizardite versus antigorite serpentinite: Magnetite, hydrogen, and life(?). *Geology*, 38(10), 879–882. <https://doi.org/10.1130/G31158.1>
- Fouquet, Y., Barriga, F., Charlou, J.-L., Elderfield, H., German, C. R., Ondreas, H., et al. (1998). FLORES diving cruise with nautilie near the Azores-first dives on the rainbow field: Hydrothermal seawater/mantle interaction. *InterRidge News*, 7, 24–28.
- Fouquet, Y., Cambon, P., Etoubleau, J., Charlou, J. L., Ondreas, H., Barriga, F. J. A. S., et al. (2010). Geodiversity of hydrothermal processes along the Mid-Atlantic Ridge and ultramafic-hosted mineralization: A new type of oceanic Cu-Zn-Co-Au volcanogenic massive sulfide deposit. *Geophysical Monograph Series*, 188, 321–367.
- Fouquet, Y., Cherkashov, G., Charlou, J. L., Ondreas, H., Birot, D., Cannat, M., et al. (2008). Serpentine cruise - Ultramafic hosted hydrothermal deposits on the Mid-Atlantic Ridge: First submersible studies on Ashadze 1 and 2, Logatchev 1 and 2, Logatchev 2 and Krasnov vent fields Contents: Fouquet_ et al_IR_News_2008_EXTENDED.pdf (Supplement p. 1-6). *InterRidge News*, 17, 16–41.
- Frey, F. A. (1980). The origin of pyroxenites and garnet pyroxenites from Salt lake crater, Oahu, Hawaii: Trace element evidence. *American Journal of Science*, 280, 427–449.
- Früh-Green, G. L., Orcutt, B. N., Rouméjon, S., Lilley, M. D., Morono, Y., Cotterill, C., et al. (2018). Magmatism, serpentinization and life: Insights through drilling the Atlantis massif (IODP expedition 357). *Lithos*, 323, 137–155. <https://doi.org/10.1016/j.lithos.2018.09.012>
- Gaggero, L., Cortesogno, L., & Gazzotti, M. (1997). 30. Data reports: Oxides, sulfides, and associated phases in veins and hydrothermally altered peridotitic rocks. In *Proceedings of the ocean drilling program, scientific results* (Vol. 153, pp. 523–529).
- Garrido, C. J., & Bodinier, J.-L. (1999). Diversity of mafic rocks in the Ronda peridotite: Evidence for pervasive melt–rock reaction during heating of subcontinental lithosphere by upwelling asthenosphere. *Journal of Petrology*, 40(5), 729–754. <https://doi.org/10.1093/petroj/40.5.729>
- Gillis, K. M., & Meyer, P. S. (2001). Metasomatism of oceanic gabbros by late stage melts and hydrothermal fluids: Evidence from the rare earth element composition of amphiboles. *Geochemistry, Geophysics, Geosystems*, 2(3), 1012. <https://doi.org/10.1029/2000GC000087>
- Godard, M., Jousset, D., & Bodinier, J.-L. (2000). Relationships between geochemistry and structure beneath a palaeo-spreading centre: A study of the mantle section in the Oman ophiolite. *Earth and Planetary Science Letters*, 180(1–2), 133–148. [https://doi.org/10.1016/s0012-821x\(00\)00149-7](https://doi.org/10.1016/s0012-821x(00)00149-7)
- Godard, M., Lagabriele, Y., Alard, O., & Harvey, J. (2008). Geochemistry of the highly depleted peridotites drilled at ODP Sites 1272 and 1274 (Fifteen-Twenty Fracture Zone, Mid-Atlantic Ridge): Implications for mantle dynamics beneath a slow spreading ridge. *Earth and Planetary Science Letters*, 267(3–4), 410–425. <https://doi.org/10.1016/j.epsl.2007.11.058>
- Grevemeyer, I., Reston, T. J., & Moeller, S. (2013). Microseismicity of the Mid-Atlantic Ridge at 7°S–8°15'S and at the Logatchev massif oceanic core complex at 14°40'N–14°50'N. *Geochemistry, Geophysics, Geosystems*, 14(9), 3532–3554. <https://doi.org/10.1002/ggge.20197>

- Guo, J., Griffin, W. L., & O'Reilly, S. Y. (1999). Geochemistry and origin of sulphide minerals in mantle xenoliths: Qilin, Southeastern China. *Journal of Petrology*, 40(7), 1125–1149. <https://doi.org/10.1093/ptro/40.7.1125>
- Gussone, N., Austrheim, H., Westhues, A., & Mezger, K. (2020). Origin of rodingite forming fluids constrained by calcium and strontium isotope ratios in the Leka ophiolite complex. *Chemical Geology*, 542, 119598. <https://doi.org/10.1016/j.chemgeo.2020.119598>
- Gustafson, W. I. (1974). The stability of andradite, hedenbergite, and related minerals in the system Ca-Fe-Si-O-H. *Journal of Petrology*, 15(3), 455–496. <https://doi.org/10.1093/ptro/15.3.455>
- Hannington, M. D., De Ronde, C. E. J., & Petersen, S. (2005). Sea-floor tectonics and submarine hydrothermal systems. *Economic Geology*, 111–141. <https://doi.org/10.5382/av100.06>
- Hannington, M. D., Jonasson, I. R., Herzig, P. M., & Petersen, S. (1995). Physical and chemical processes of seafloor mineralization at Mid-Ocean Ridges. *Geophysical Monograph Series*, 91, 115–157.
- Hébert, R., Adamson, C. A., & Komor, S. C. (1990). Metamorphic petrology of ODP Leg 109, hole 670A serpentinized peridotites: Serpentinization processes at a slow spreading ridge environment. In *Proceedings of the ocean drilling program, scientific results* (pp. 103–115). Ocean Drilling Program.
- Horning, G., Sohn, R. A., Canales, J. P., & Dunn, R. A. (2018). Local seismicity of the rainbow massif on the Mid-Atlantic Ridge. *Journal of Geophysical Research: Solid Earth*, 123(2), 1615–1630. <https://doi.org/10.1002/2017jb015288>
- Howie, R. A., Zussman, J., & Deer, W. (1992). *An introduction to the rock-forming minerals*. Longman London.
- Hu, L.-Z., Kang, J.-T., Qi, Y.-H., Gao, Y.-J., Nan, X.-Y., Huang, J., & Huang, F. (2023). Calcium isotope systematics of altered oceanic crust at IODP site 1256: Insights into the hydrothermal alteration. *Lithos*, 438–439, 106994. <https://doi.org/10.1016/j.lithos.2022.106994>
- Ionov, D. A., Savoyant, L., & Dupuy, C. (1992). Application of the ICP-MS technique to trace element analysis of peridotites and their minerals. *Geostandards Newsletter*, 16(2), 311–315. <https://doi.org/10.1111/j.1751-908x.1992.tb00494.x>
- Jagoutz, E., Palme, H., Baddenhausen, H., Blum, K., Cendales, M., Dreibus, G., et al. (1979). The abundances of major, minor and trace elements in the Earth's mantle as derived from primitive ultramafic nodules. In *Lunar and planetary science conference Proceedings* (pp. 2031–2050).
- Jochum, K. P., Seufert, H. M., & Thirlwall, M. F. (1990). High-sensitivity Nb analysis by spark-source mass spectrometry (SSMS) and calibration of XRF Nb and Zr. *Chemical Geology*, 81(1–2), 1–16. [https://doi.org/10.1016/0009-2541\(90\)90035-6](https://doi.org/10.1016/0009-2541(90)90035-6)
- Kang, J.-T., Ionov, D. A., Liu, F., Zhang, C.-L., Golovin, A. V., Qin, L.-P., et al. (2017). Calcium isotopic fractionation in mantle peridotites by melting and metasomatism and Ca isotope composition of the Bulk Silicate Earth. *Earth and Planetary Science Letters*, 474, 128–137. <https://doi.org/10.1016/j.epsl.2017.05.035>
- Kelemen, P. B., Kikawa, E., Miller, D. J., & Party, S. S. (2007). Leg 209 summary: Processes in a 20-km-thick conductive boundary layer beneath the Mid-Atlantic Ridge, 14–16 N. In *Proceedings of the ocean drilling program, scientific results* (pp. 1–33). Ocean Drilling Program.
- Kelley, D. S., Karson, J. A., Blackman, D. K., Früh-Green, G. L., Butterfield, D. A., Lilley, M. D., et al. (2001). An off-axis hydrothermal vent field near the Mid-Atlantic Ridge at 30°N. *Nature*, 412(6843), 145–149. <https://doi.org/10.1038/35084000>
- Kim, J., Son, S., Kim, D., Pak, S., Yu, O. H., Walker, S. L., et al. (2020). Discovery of active hydrothermal vent fields along the Central Indian Ridge, 8–12 S. *Geochemistry, Geophysics, Geosystems*, 21(8), e2020GC009058. <https://doi.org/10.1029/2020gc009058>
- Klinkhammer, G. P., Elderfield, H., Edmond, J. M., & Mitra, A. (1994). Geochemical implications of rare earth element patterns in hydrothermal fluids from mid-ocean ridges. *Geochimica et Cosmochimica Acta*, 58(23), 5105–5113. [https://doi.org/10.1016/0016-7037\(94\)90297-6](https://doi.org/10.1016/0016-7037(94)90297-6)
- Krasnov, S. G., Cherkashev, G. A., Stepanova, T. V., Batuyev, B. N., Krotov, A. G., Malin, B. V., et al. (1995). Detailed geological studies of hydrothermal fields in the North Atlantic. *Geological Society, London, Special Publications*, 87(1), 43–64. <https://doi.org/10.1144/gsl.sp.1995.087.01.05>
- Liao, Y., Wei, C., & Rehman, H. U. (2021). Titanium in calcium amphibole: Behavior and thermometry. *American Mineralogist*, 106(2), 180–191. <https://doi.org/10.2138/am-2020-7409>
- Macleod, C. J., Searle, R. C., Murton, B. J., Casey, J. F., Mallows, C., Unsworth, S. C., et al. (2009). Life cycle of oceanic core complexes. *Earth and Planetary Science Letters*, 287(3–4), 333–344. <https://doi.org/10.1016/j.epsl.2009.08.016>
- Mallows, C., & Searle, R. C. (2012). A geophysical study of oceanic core complexes and surrounding terrain, Mid-Atlantic Ridge 13°N–14°N. *Geochemistry, Geophysics, Geosystems*, 13(6), Q0AG08. <https://doi.org/10.1029/2012GC004075>
- Marques, A. F. A., Barriga, F. J. A. S., Chavagnac, V., & Fouquet, Y. (2006). Mineralogy, geochemistry, and Nd isotope composition of the rainbow hydrothermal field, Mid-Atlantic Ridge. *Mineralium Deposita*, 41(1), 52–67. <https://doi.org/10.1007/s00126-005-0040-8>
- Marques, A. F. A., Barriga, F. J. A. S., & Scott, S. D. (2007). Sulfide mineralization in an ultramafic-rock hosted seafloor hydrothermal system: From serpentinization to the formation of Cu–Zn–(Co)-rich massive sulfides. *Marine Geology*, 245(1–4), 20–39. <https://doi.org/10.1016/j.margeo.2007.05.007>
- McCaig, A. M., Cliff, R. A., Escartín, J., Fallick, A. E., & MacLeod, C. J. (2007). Oceanic detachment faults focus very large volumes of black smoker fluids. *Geology*, 35(10), 935–938. <https://doi.org/10.1130/G23657A.1>
- McCaig, A. M., Delacour, A., Fallick, A. E., Castelain, T., & Früh-Green, G. L. (2010). Detachment Fault control on hydrothermal circulation systems: Interpreting the subsurface beneath the TAG hydrothermal field using the isotopic and geological evolution of oceanic core complexes in the Atlantic. *Geophysical Monograph Series*, 188, 207–239. <https://doi.org/10.1029/2008GM000729>
- McDonough, W. F., & Sun, S. S. (1995). The composition of the Earth. *Chemical Geology*, 120(3–4), 223–253. [https://doi.org/10.1016/0009-2541\(94\)00140-4](https://doi.org/10.1016/0009-2541(94)00140-4)
- Melchert, B., Devey, C. W., German, C. R., Lackschewitz, K. S., Seifert, R., Walter, M., et al. (2008). First evidence for high-temperature off-axis venting of deep crustal/mantle heat: The Nibelungen hydrothermal field, southern Mid-Atlantic Ridge. *Earth and Planetary Science Letters*, 275(1–2), 61–69. <https://doi.org/10.1016/j.epsl.2008.08.010>
- Melekestseva, I. Y., Zaykov, V. V., Nimis, P., Tret' Yakov, G. A., & Tessalina, S. G. (2013). Cu–(Ni–Co–Au)-bearing massive sulfide deposits associated with mafic–ultramafic rocks of the Main Urals Fault, South Urals: Geological structures, ore textural and mineralogical features, comparison with modern analogs. *Ore Geology Reviews*, 52, 18–36. <https://doi.org/10.1016/j.oregeorev.2012.03.005>
- Moody, J. B. (1976). Serpentinization: A review. *Lithos*, 9(2), 125–138. [https://doi.org/10.1016/0024-4937\(76\)90030-x](https://doi.org/10.1016/0024-4937(76)90030-x)
- Niida, K. (1997). 12, mineralogy of mark peridotites: Replacement through magma chaneling examined from hole 920D, mark area. In *Proceedings of ocean drilling program*.
- Ondréas, H., Cannat, M., Fouquet, Y., & Normand, A. (2012). Geological context and vents morphology of the ultramafic-hosted Ashadze hydrothermal areas (Mid-Atlantic Ridge 13°N). *Geochemistry, Geophysics, Geosystems*, 13(11), 1–20. <https://doi.org/10.1029/2012GC004433>
- Parnell-Turner, R., Sohn, R. A., Peirce, C., Reston, T. J., MacLeod, C. J., Searle, R. C., & Simão, N. M. (2017). Oceanic detachment faults generate compression in extension. *Geology*, 45(10), 923–926. <https://doi.org/10.1130/G39232.1>
- Patten, C. G. C., Coltat, R., Junge, M., Peillod, A., Ulrich, M., Manatschal, G., & Kolb, J. (2022). Ultramafic-hosted volcanogenic massive sulfide deposits: An overlooked sub-class of VMS deposit forming in complex tectonic environments. *Earth-Science Reviews*, 224, 103891. <https://doi.org/10.1016/j.earscirev.2021.103891>

- Patten, C. G. C., Pitcairn, I. K., Teagle, D. A., & Harris, M. (2015). Mobility of Au and related elements during the hydrothermal alteration of the oceanic crust: Implications for the sources of metals in VMS deposits. *Mineralium Deposita*, 51(2), 1–22. <https://doi.org/10.1007/s00126-015-0598-8>
- Patten, C. G. C., Pitcairn, I. K., Teagle, D. A. H., & Harris, M. (2016). Sulphide mineral evolution and metal mobility during alteration of the oceanic crust: Insights from ODP Hole 1256D. *Geochimica et Cosmochimica Acta*, 193, 132–159. <https://doi.org/10.1016/j.gca.2016.08.009>
- Paulick, H., Bach, W., Godard, M., Hoog, J. C. M., De Suhr, G., & Harvey, J. (2006). Geochemistry of abyssal peridotites (Mid-Atlantic Ridge, 15°20'N, ODP Leg 209): Implications for fluid/rock interaction in slow spreading environments. *Chemical Geology*, 234(3–4), 179–210. <https://doi.org/10.1016/j.chemgeo.2006.04.011>
- Pedersen, R. B., Thorseth, I. H., Nygård, T. E., Lilley, M. D., & Kelley, D. S. (2010). Hydrothermal activity at the Arctic Mid-Ocean Ridges. *Divers Hydrothermal Syst Slow Spreading Ocean Ridges*, 188, 67–89.
- Peltonen, P., Kontinen, A., Huhma, H., & Kuronen, U. (2008). Outokumpu revisited: New mineral deposit model for the mantle peridotite-associated Cu–Co–Zn–Ni–Ag–Au sulphide deposits. *Ore Geology Reviews*, 33(3–4), 559–617. <https://doi.org/10.1016/j.oregeorev.2007.07.002>
- Petersen, S., Kuhn, K., Kuhn, T., Augustin, N., Hékinian, R., Franz, L., & Borowski, C. (2009). The geological setting of the ultramafic-hosted Logatchev hydrothermal field (14°45'N, Mid-Atlantic Ridge) and its influence on massive sulfide formation. *Lithos*, 112(1–2), 40–56. <https://doi.org/10.1016/j.lithos.2009.02.008>
- Potrasson, F., Delpech, G., & Grégoire, M. (2013). On the iron isotope heterogeneity of lithospheric mantle xenoliths: Implications for mantle metasomatism, the origin of basalts and the iron isotope composition of the earth. *Contributions to Mineralogy and Petrology*, 165(6), 1243–1258. <https://doi.org/10.1007/s00410-013-0856-7>
- Reed, M. H., & Palandri, J. (2006). Sulfide mineral precipitation from hydrothermal fluids. *Reviews in Mineralogy and Geochemistry*, 61(1), 609–631. <https://doi.org/10.2138/rmg.2006.61.11>
- Rouméljon, S., & Cannat, M. (2014). Serpentinization of mantle-derived peridotites at mid-ocean ridges: Mesh texture development in the context of tectonic exhumation. *Geochemistry, Geophysics, Geosystems*, 15(6), 2354–2379. <https://doi.org/10.1002/2013GC005148>. Received
- Rouxel, O., Fouquet, Y., & Ludden, J. N. (2004a). Copper isotope systematics of the lucky strike, rainbow, and Logatchev sea-floor hydrothermal fields on the Mid-Atlantic Ridge. *Economic Geology*, 99(3), 585–600. <https://doi.org/10.2113/gsecongeo.99.3.585>
- Rouxel, O., Fouquet, Y., & Ludden, J. N. (2004b). Subsurface processes at the lucky strike hydrothermal field, Mid-Atlantic Ridge: Evidence from sulfur, selenium, and iron isotopes. *Geochimica et Cosmochimica Acta*, 68(10), 2295–2311. <https://doi.org/10.1016/j.gca.2003.11.029>
- Sahlström, F., Palinkaš, S. S., Dundas, S. H., Sendula, E., Cheng, Y., Wold, M., & Pedersen, R. B., (2022). Mineralogical distribution and genetic aspects of cobalt at the active Fåvne and Loki's Castle seafloor massive sulfide deposits, Arctic Mid-Ocean Ridges. In *Ore geol rev 105261*.
- Schulz, N. J., Detrick, R. S., & Miller, S. P. (1988). Two- and three-dimensional inversions of magnetic anomalies in the MARK area (Mid-Atlantic Ridge 23 N). *Marine Geophysical Researches*, 10(1–2), 41–57. <https://doi.org/10.1007/bf02424660>
- Schwarzenbach, E. M., & Steele-MacInnis, M. (2020). Fluids in submarine mid-ocean ridge hydrothermal settings. *Elements: An International Magazine of Mineralogy, Geochemistry, and Petrology*, 16(6), 389–394. <https://doi.org/10.2138/gselements.16.6.389>
- Sohrin, Y., Iwamoto, S. I., Akiyama, S., Fujita, T., Kugii, T., Obata, H., et al. (1998). Determination of trace elements in seawater by fluorinated metal alkoxide glass-immobilized 8-hydroxyquinoline concentration and high-resolution inductively coupled plasma mass spectrometry detection. *Analytica Chimica Acta*, 363(1), 11–19. [https://doi.org/10.1016/S0003-2670\(98\)00074-9](https://doi.org/10.1016/S0003-2670(98)00074-9)
- Sossi, P. A., Nebel, O., O'Neill, H. S. C., & Moynier, F. (2018). Zinc isotope composition of the Earth and its behaviour during planetary accretion. *Chemical Geology*, 477, 73–84. <https://doi.org/10.1016/j.chemgeo.2017.12.006>
- Stephens, C. J. (1997). Heterogeneity of oceanic peridotite from the western canyon wall at MARK: Results from site 920. In *Proceedings of the ocean drilling program* (pp. 285–303). Scientific Results.
- Szitar, F., Dymant, J., Fouquet, Y., Honsho, C., & Horen, H. (2014). The magnetic signature of ultramafic-hosted hydrothermal sites. *Geology*, 42(8), 715–718. <https://doi.org/10.1130/G35729.1>
- Tao, C., Li, H., Jin, X., Zhou, J., Wu, T., He, Y., et al. (2014). Seafloor hydrothermal activity and polymetallic sulfide exploration on the southwest Indian ridge. *Chinese Science Bulletin*, 59(19), 2266–2276. <https://doi.org/10.1007/s11434-014-0182-0>
- Teng, F.-Z., Dauphas, N., Helz, R. T., Gao, S., & Huang, S. (2011). Diffusion-driven magnesium and iron isotope fractionation in Hawaiian olivine. *Earth and Planetary Science Letters*, 308(3–4), 317–324. <https://doi.org/10.1016/j.epsl.2011.06.003>
- Tilhac, R., Ceuleneer, G., Griffin, W. L., O'Reilly, S. Y., Pearson, N. J., Benoit, M., et al. (2016). Primitive arc magmatism and delamination: Petrology and geochemistry of pyroxenites from the Cabo Ortegal complex, Spain. *Journal of Petrology*, 57(10), 1921–1954. <https://doi.org/10.1093/petrology/egw064>
- Tilmann, F., Flueh, E., Planert, L., Reston, T., & Weinrebe, W. (2004). Microearthquake seismicity of the Mid-Atlantic Ridge at 5 S: A view of tectonic extension. *Journal of Geophysical Research*, 109(B6), B06102. <https://doi.org/10.1029/2003jb002827>
- Toffolo, L., Nimis, P., Martín, S., Tumiati, S., & Bach, W. (2017). The Cogne magnetite deposit (Western Alps, Italy): A late Jurassic seafloor ultramafic-hosted hydrothermal system? *Ore Geology Reviews*, 83, 103–126. <https://doi.org/10.1016/j.oregeorev.2016.11.030>
- Tucholke, E., Lin, J., & Kleinrock, C. (1998). Megamullions and mullion structure defining oceanic metamorphic core complexes on the Mid-Atlantic Ridge. *Journal of Geophysical Research*, 103(B5), 9857–9866. <https://doi.org/10.1029/98jb00167>
- Verlaquet, A., Bonnemains, D., Mével, C., Escartín, J., Andreani, M., Bourdelle, F., et al. (2021). Fluid circulation along an oceanic detachment fault: Insights from fluid inclusions in silicified brecciated fault rocks (Mid-Atlantic Ridge at 13°20'N). *Geochemistry, Geophysics, Geosystems*, 22(1), e2020GC009235. <https://doi.org/10.1029/2020gc009235>
- Vití, C., & Mellini, M. (1998). Mesh textures and bastites in the Elba retrograde serpentinites. *European Journal of Mineralogy*, 10(6), 1341–1359. <https://doi.org/10.1127/ejm/10/6/1341>
- Wang, Y., Han, X., Petersen, S., Jin, X., Qiu, Z., & Zhu, J. (2014). Mineralogy and geochemistry of hydrothermal precipitates from Kairei hydrothermal field, Central Indian Ridge. *Marine Geology*, 354, 69–80. <https://doi.org/10.1016/j.margeo.2014.05.003>
- Wang, Z.-Z., Liu, S.-A., Liu, J., Huang, J., Xiao, Y., Chu, Z.-Y., et al. (2017). Zinc isotope fractionation during mantle melting and constraints on the Zn isotope composition of Earth's upper mantle. *Geochimica et Cosmochimica Acta*, 198, 151–167. <https://doi.org/10.1016/j.gca.2016.11.014>
- Werner, C.-D., & Pilot, J. (1997). 26. Data report: Geochemistry and mineral chemistry of ultramafic rocks from the Kane Area (MARK). In *Proc ocean drilling program, Sci results* (pp. 457–470).
- Weyer, S., & Ionov, D. A. (2007). Partial melting and melt percolation in the mantle: The message from Fe isotopes. *Earth and Planetary Science Letters*, 259(1–2), 119–133. <https://doi.org/10.1016/j.epsl.2007.04.033>
- Wolfe, C. J., Purdy, G. M., Toomey, D. R., & Solomon, S. C. (1995). Microearthquake characteristics and crustal velocity structure at 29°N on the Mid-Atlantic Ridge: The architecture of a slow spreading segment. *Journal of Geophysical Research*, 100(B12), 24449–24472. <https://doi.org/10.1029/95jb02399>

- Zhang, C., Koepke, J., Wolff, P. E., Horn, I., Garbe-Schönberg, D., & Berndt, J. (2021). Multi-stage hydrothermal veins in layered gabbro of the Oman ophiolite: Implications for focused fluid circulation in the lower oceanic crust. *Journal of Geophysical Research: Solid Earth*, 126(8), e2021JB022349. <https://doi.org/10.1029/2021jb022349>
- Zhao, M., Canales, J. P., & Sohn, R. A. (2012). Three-dimensional seismic structure of a Mid-Atlantic Ridge segment characterized by active detachment faulting (Trans-Atlantic Geotraverse, 25°55'N–26°20'N). *Geochemistry, Geophysics, Geosystems*, 13(11), Q0AG13. <https://doi.org/10.1029/2012gc004454>

References From the Supporting Information

- Morimoto, N. (1988). Nomenclature of pyroxenes. *Mineralogy and Petrology*, 39(1), 55–76. <https://doi.org/10.1007/bf01226262>